Inorganic Chemistry
Cite This: Inorg. Chem. 2019, 58, 8969−8982
Article
pubs.acs.org/IC

A Biochemical Nickel(I) State Supports Nucleophilic Alkyl Addition: A Roadmap for Methyl Reactivity in Acetyl Coenzyme A Synthase

Anastasia C. Manesis,[†] Bradley W. Musselman,[§] Brenna C. Keegan,[⊥] Jason Shearer,[⊥] Nicolai Lehnert,[§] and Hannah S. Shafaat*,[†]

[†]Department of Chemistry and Biochemistry, The Ohio State University, 100 W. 18th Avenue, Columbus, Ohio 43210, United States
[§]Department of Chemistry, University of Michigan, 930 N. University Avenue, Ann Arbor, Michigan 48109, United States
[⊥]Department of Chemistry, Trinity University, One Trinity Place, San Antonio, Texas 78212, United States

Supporting Information

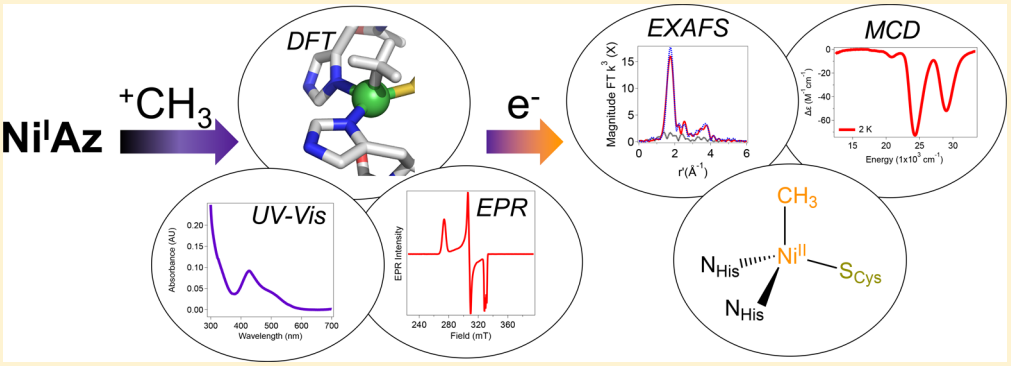

ABSTRACT: Nickel-containing enzymes such as methyl coenzyme M reductase (MCR) and carbon monoxide dehydrogenase/acetyl coenzyme A synthase (CODH/ACS) play a critical role in global energy conversion reactions, with significant contributions to carbon-centered processes. These enzymes are implied to cycle through a series of nickel-based organometallic intermediates during catalysis, though identification of these intermediates remains challenging. In this work, we have developed and characterized a nickel-containing metalloprotein that models the methyl-bound organometallic intermediates proposed in the native enzymes. Using a nickel(I)-substituted azurin mutant, we demonstrate that alkyl binding occurs via nucleophilic addition of methyl iodide as a methyl donor. The paramagnetic Ni^{III}-CH_3 species initially generated can be rapidly reduced to a high-spin Ni^{II}-CH_3 species in the presence of exogenous reducing agent, following a reaction sequence analogous to that proposed for ACS. These two distinct bioorganometallic species have been characterized by optical, EPR, XAS, and MCD spectroscopy, and the overall mechanism describing methyl reactivity with nickel azurin has been quantitatively modeled using global kinetic simulations. A comparison between the nickel azurin protein system and existing ACS model compounds is presented. Ni^{III}-CH_3 Az is only the second example of two-electron addition of methyl iodide to a Ni^{I} center to give an isolable species and the first to be formed in a biologically relevant system. These results highlight the divergent reactivity of nickel across the two intermediates, with implications for likely reaction mechanisms and catalytically relevant states in the native ACS enzyme.

INTRODUCTION

Nickel enzymes are responsible for some of the most important energy conversion reactions found in nature, specifically those relevant to carbon-centered processes.[1−3] Within the environment, one-carbon species such as CO, CO_2, and CH_4 are continually interconverted through nickel-dependent gas cycles. The selection of nickel to accomplish such challenging organic transformations within anaerobic archaea and bacteria implicates its use in primordial life processes, particularly when considering the high concentrations of nickel in the earth's early oceans and the broad reactivity of nickel with reduced, sulfur-containing compounds.[4−8] The global carbon cycle relies heavily on three enzymes. The Ni-containing F_{430} cofactor of methyl coenzyme M reductase (MCR) is used extensively in anaerobic methane conversion reactions, responsible for the production of over one billion tons of methane per year.[9] This enzyme is also capable of catalyzing methane oxidation, another highly sought after reaction. The Ni-containing active sites of the carbon monoxide dehydrogenase (CODH) and acetyl coenzyme A synthase (ACS) enzymes occupy a central role in the metabolisms of anaerobic bacteria and archaea, catalyzing the reversible synthesis of acetyl-CoA from carbon dioxide and a

Received: December 20, 2018
Published: February 21, 2019

DOI: 10.1021/acs.inorgchem.8b03546
Inorg. Chem. 2019, 58, 8969−8982

methyl group.[10−12] It has been suggested that these enzymes cycle through a series of nickel-based organometallic intermediates during catalysis (Figure 1); however, the

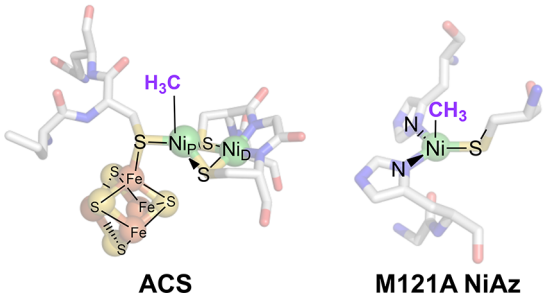

Figure 1. Proposed nickel methyl intermediates in ACS and NiAz.

reactivity of nickel varies greatly in each enzyme, with different products formed from the use of similar building blocks. This diverse chemistry is unsurprising given the distinct coordination environments around nickel in each enzyme.

A closer look at the catalytic mechanisms for both ACS and MCR reveals ambiguity regarding nickel oxidation states and unresolved intermediates. In the case of ACS, one proposed mechanism suggests a catalytically relevant Ni_P^I state is required for activity.[12−15] Because it has been shown that the reactive methyl group in ACS is transferred as a cationic species from a cobalt corrinoid protein, this paramagnetic mechanism implicates an organometallic Ni_P^{III}-CH_3 species as a catalytic intermediate (if only transiently formed). Alternatively, it has been suggested that a Ni_P^I state could not support addition of a cationic methyl group on the basis of comparison to small molecule models in organic solvents. This mechanism requires the active state of ACS to be two electrons more reduced than that of the as-isolated, Ni^{II} A_{ox} state and necessitates only a Ni_P^{II}-CH_3 species.[16,17] On the other hand, a square pyramidal Ni^{III}-CH_3 species in MCR has been trapped and characterized using electron paramagnetic resonance (EPR) spectroscopy,[18−22] though studies suggest this state is not relevant for catalysis.[23,24] With such ongoing debate, a biochemical model system that can reproduce the structures of potentially relevant organometallic intermediates may shed light on these complex systems, deepening our understanding of organonickel reactions in nature and offering opportunities to develop organometallic reactions using simple nickel compounds.

Previous work has demonstrated the use of a nickel-substituted mutant (M121A) of *Pseudomonas aeruginosa* azurin to generate an isolable Ni^I center with an open coordination site capable of interacting with exogenous ligands, including CO and $-CH_3$ groups, which are the two putatively metal-bound ACS substrates.[25] The Ni^I-CO species was characterized using optical, vibrational, and EPR spectroscopy, and reaction of Ni^IAz with CH_3I resulted in an EPR-silent NiAz species. Moreover, a Ni^{III}Az state was generated and characterized by EPR. Because of the potential capability to participate in multielectron chemistry, M121A NiAz has been further developed as a model system for ACS. The reactivity of M121A Ni^IAz with biologically relevant methyl donors has been investigated, and the elusive Ni^{III}-CH_3 state has been generated and trapped, supporting the analogy of M121A NiAz as a biochemical model for ACS. The structure and reactivity of this state have been characterized using an array of techniques, including time-resolved optical and EPR spectroscopies as well as computational analyses. Additionally, the Ni^{II}-CH_3 Az species has been interrogated with resonance Raman, magnetic circular dichroism (MCD), and X-ray spectroscopy to refine the geometric and electronic structure, and this state has been shown to react further with CO. Methane is found to be the sole reaction product following CH_3I addition, indicating this system is incapable of supporting hydrolysis, drawing further analogies to reactions seen in methylated ACS and MCR. Together, these results have implications for the order of substrate addition and relevant oxidation states for the organometallic reactions performed by ACS.

RESULTS

Rapidly Mixing M121A Ni^IAz with CH_3I Reveals Transient Nickel-Centered Signals Using Optical Spectroscopy. Reduction of M121A Ni^{II}Az with 50 mM Eu^{II}DTPA results in complete conversion to M121A Ni^IAz, as previously reported, which can react with CO or CH_3I.[25] However, in our prior work, the presence of significant amounts of excess reducing agent in solution prevented observation of a Ni^{III}-CH_3 state, which is expected to exhibit a high reduction potential and be rapidly reduced by residual Eu^{II}DTPA. Moreover, methyl iodide can react with nucleo-

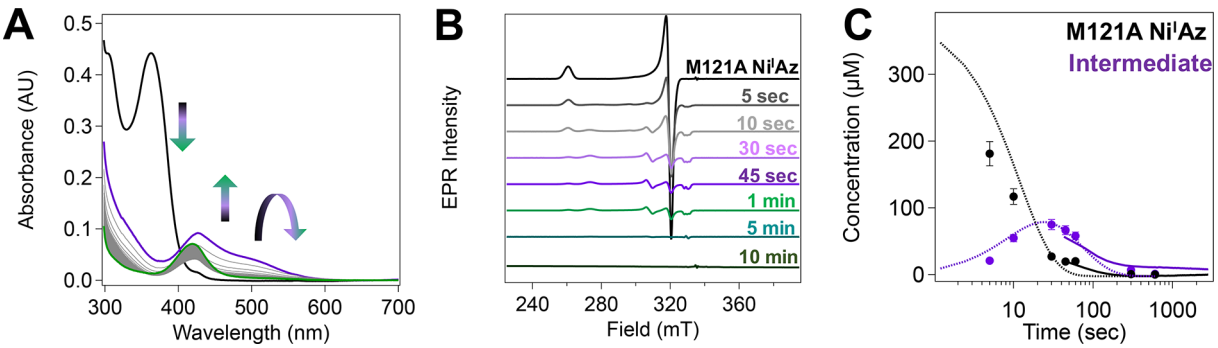

Figure 2. Rapid mixing of M121A Ni^IAz with CH_3I. (A) UV−vis traces after rapidly mixing an aliquot of CH_3I to a final concentration of 1.5 mM into 300 μM M121A Ni^IAz (initial trace shown in black). Sample was prepared in 50 mM phosphate buffer, pH 8.0. Spectra were taken every 35 s after mixing. (B) CW X-band EPR spectra after rapidly mixing an aliquot of CH_3I to a final concentration of 1.5 mM into 300 μM M121A Ni^IAz, quenched at indicated time points. Samples were prepared in 50 mM phosphate buffer, pH 8.0. (C) Concentrations determined from UV−vis absorption (solid lines) and EPR (circles) experiments for M121A Ni^IAz (black), and the intermediate (purple) overlaid on the fit from the proposed kinetic model (dotted lines).

DOI: 10.1021/acs.inorgchem.8b03546
Inorg. Chem. 2019, 58, 8969−8982

philes through either a two-electron or a radical pathway, leading to questions about the nature of the methyl transfer and the product formed. To address these issues and resolve the capacity of a biological Ni^{I} center to support nucleophilic attack on a cationic carbon center, which remains an outstanding question for the mechanism of ACS, a hand-packed, small-volume desalting column was generated. When combined with low-speed centrifugal filter concentration, this preparation removes most of the excess Eu^{II}DTPA, leaving a solution of pure M121A Ni^{I}Az with only minimal residual reducing agent present (Figure S1). A spectroscopically silent methyl donor is necessary to trap and characterize the products of methyl transfer to M121A Ni^{I}Az. Due to rapid hydrolysis of methyl triflate in aqueous solution,[26,27] which precludes reaction with M121A Ni^{I}Az (Figure S2), methyl iodide was again selected as a methylating agent for spectroscopic studies on Ni-CH_3 Az species, despite the potential for multiple reaction pathways.

Rapid mixing experiments with CH_3I revealed the formation of a transient optical signal centered at 488 nm that rises and decays on the time scale of seconds and minutes, respectively, with kinetics that are dependent on the concentration of CH_3I (Figure 2A). This feature decays into a signal with similar features as the M121A Ni^{II}Az state, with an isosbestic point for the later transition indicating a one-to-one conversion (Figure 2A). Increasing amounts of CH_3I accelerate the decay of Ni^{I}Az as well as rates and amount of formation of the new species (Figure S3), while addition of exogenous Eu^{II}DTPA decreases the amount of transient species observed (Figure S4). This is consistent with our prior results, in which our inability to resolve any transient species after methyl addition was attributed to the presence of 10−50 mM Eu^{II}DTPA. Singular value decomposition (SVD) analysis of the UV−vis spectra as a function of time, substrate, and reductant concentration reveals four distinct components, including two transient ones, that contribute to the overall spectra (Figure S5). As such, the proposed reaction model incorporated these observables. Global fitting (Figure S5) of the kinetic profiles of each of the components was used to extract the elementary rate constants and effective solvent kinetic isotope effects (KIEs).

No new absorption features were observed to appear upon mixing of CH_3I with $NiSO_4$ and EuDTPA, metal-free (apo-) Az, or Ni^{II}Az in phosphate buffer at pH 8.0 (Figure S6), suggesting that the features seen in the M121A Ni^{I}Az mixing experiments are due to an interaction of the methyl donor with the protein-loaded Ni^{I} center. Additional control experiments using ^{13}C NMR indicate that CH_3I is stable toward hydrolysis over at least 1 h, which is more than sufficient for the time scale of the experiments performed in this work (Figure S7).

The addition of longer, less reactive alkylating agents, such as ethyl iodide, results in the same intermediate species, albeit formed at much slower rates and in lower quantities (Figure S8). By holding the alkyl group constant and changing the leaving group from an iodide to a bromide, the decay of M121A Ni^{I}Az is further slowed, and even lower concentrations of intermediate accumulate in the UV−vis (Figure S9). Recognizing that an ethyl radical is more stable than a methyl radical, these observations suggest that alkyl addition is favored to occur via nucleophilic attack rather than a radical-based mechanism.

EPR Spectroscopy Confirms the Generation of a Bioorganometallic Ni^{III}-CH_3 Species. To examine whether the interaction between M121A Ni^{I}Az and CH_3I proceeds via cationic or radical methyl addition and identify the nature of the transient species, EPR spectroscopy was performed on freeze-quenched samples. An aliquot of CH_3I was rapidly mixed into M121A Ni^{I}Az, and EPR samples were frozen using an isopentane-liquid nitrogen bath at various time points. The CW X-band EPR spectra of these samples measured at 30 K reveal the formation of a new, EPR-active species with *g*-values of 2.46, 2.18, and 2.04. The signal is maximized at 45 s and begins to decrease after that point (Figure 2B). Formation and decay of the EPR features correlate with the formation and decay of the UV−vis band at 488 nm, suggesting the signals derive from the same transient species (Figure 2C). The *g*-values and relaxation properties indicate that the EPR-active signal arises from a low-spin, nickel-centered species (Figure S10).[28]

Experiments using isotopically substituted CH_3I support a direct interaction of the methyl group with the nickel center. Samples prepared with natural abundance CH_3I show well-defined splitting on the high-field turning point into three peaks separated by ∼40 MHz, characteristic of coupling to a single I = 1 nucleus (e.g., ^{14}N from a histidine residue). When samples are prepared using isotopically labeled $^{13}CH_3I$ (Figure S11), additional line broadening is seen across the spectrum (Figure 3). Specifically, substantial coupling on the high-field turning point obscures the three well-defined peaks, and the midfield feature at 310 mT is also visibly broadened (Figure S12).[29−31] The low-field turning point exhibits greater line broadening in all isotopes than is typical, likely due to *g*-strain,

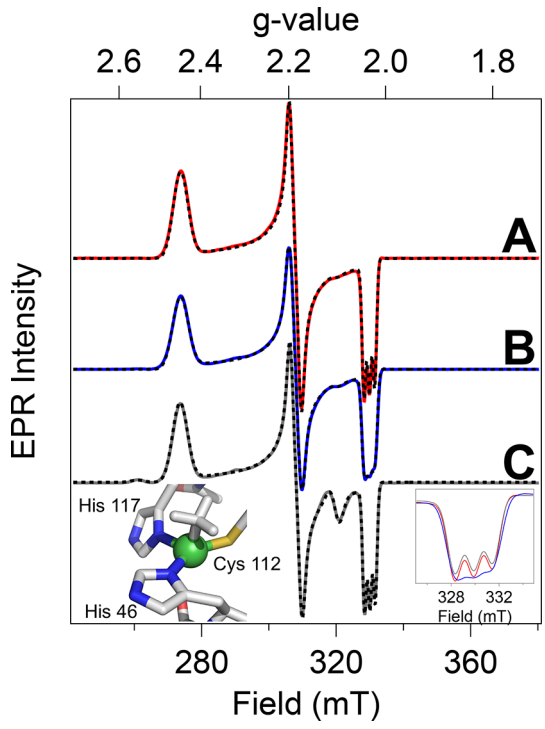

Figure 3. CW X-band EPR spectra of the M121A Ni^{III}-CH_3 Az intermediate. EPR spectra (T = 30 K; $P_{\mu w}$ = 0.2 mW) of ∼2 mM M121A Ni^{I}Az rapidly mixed with 100 mM (A) CH_3I (red), (B) $^{13}CH_3I$ (blue), and (C) CD_3I (gray) and frozen after 45 s. Samples contained 30% glycerol in 50 mM phosphate buffer, pH 8.0. Simulations overlaid on traces as dotted lines. (Left inset) Gas-phase optimized geometry of M121A Ni^{III}-CH_3 Az. (Right inset) Zoomed-in view of high-field turning point for the isotopically labeled substrates.

DOI: 10.1021/acs.inorgchem.8b03546
Inorg. Chem. 2019, 58, 8969−8982

and added interactions between a ^{13}C center are not well-resolved. Experiments performed using CD_3I (Figure S12) show very slight narrowing across the spectrum, possibly suggesting weak coupling to the methyl-derived protons (Figure 3), though high-resolution pulsed EPR studies will be necessary to resolve these small, secondary interactions.

To reproduce the observed spectral features, the CW EPR spectrum is simulated with a 45 MHz coupling constant to a nitrogen nucleus along the high-field feature and one additional, large coupling constant of 21 MHz in the $^{13}CH_3I$ samples (Table 1), comparable to the 18 MHz hyperfine coupling reported for $^{13}CH_3$-bound MCR.[18] Similarly, the broadening at the center field position necessitates inclusion of an additional 30 MHz coupling constant. That this significant coupling can be clearly resolved in the CW-EPR spectrum of this species confirms that the new signal can be assigned to a Ni^{III}-CH_3 Az state, representing only the second biochemical Ni^{III}-CH_3 species ever identified and the first not found within a redox-active, macrocyclic environment.[22] Analogous experiments with ethyl iodide and ethyl bromide result in small quantities of EPR-active intermediate, supporting the electrophilic addition of an alkyl cation to the metal center rather than a radical addition process (Figure S13).

Table 1. Select Structural and Spectroscopic Metrics for M121A Ni^{III}-CH_3 and Ni^{II}-CH_3 Az[a]

structural metrics	Ni-Cys_{112} (Å)	Ni-His_{117} (Å)	Ni-His_{46} (Å)	Ni-C_{CH3} (Å)	Ni-S_{cys}-N_{His117}-N_{His46} (deg)
calcd Ni^{III}-CH_3	2.18	2.05	1.98	1.95	+5.6
calcd Ni^{II}-CH_3	2.29	2.06	2.09	2.01	+35.2
expt. Ni^{II}Az	2.17	1.94	1.94	NA	
expt. Ni^{II}-CH_3	2.24	2.02	2.02	1.92	

g-tensor	g_1	g_2	g_3	g_{iso}
expt.	2.46	2.18	2.04	2.23
calcd	2.25	2.19	2.07	2.17

hyperfine coupling constants	atom	$\|A_1\|$[b] (MHz)	$\|A_2\|$ (MHz)	$\|A_3\|$ (MHz)	$\|A_{iso}\|$[b] (MHz)
expt.	^{14}N	NR	36	45	NR
	^{13}C	NR	30	21	NR
calcd	^{14}N His_{117}	36.6	37.6	47.3	40.5
	^{14}N His_{46}	9.0	9.1	13.1	10.4
	$^{13}CH_3$	−39.3	−39.7	−73.7	−50.9

[a]Calculated bond lengths, Ni^{III}-CH_3 Az *g*-tensor values, and Ni^{III}-CH_3 Az hyperfine coupling constants compared to experimental values. [b]"NR" stands for not resolved due to unresolved broadening on the low-field turning point.

Density Functional Theory Calculations Support Assignment of the Transient Species to a Ni^{III}-CH_3 State. Geometry optimizations using density functional theory (DFT) of a Ni^{III}-CH_3 center within a cluster model of the azurin active site show a distorted trigonal pyramidal center, with the nickel atom pulled only slightly out of the plane of the trigonal $(His)_2Cys$ ligand framework (Figure 3, inset; Table 1). The symmetry between the two histidine ligands appears to be broken, with one Ni−N_{His46} distance of 1.98 Å and the other Ni−N_{His117} distance of 2.05 Å. The Ni−S_{Cys112} bond distance remains short, at 2.16 Å, and a short Ni−C bond of 1.95 Å completes the primary coordination sphere (Table 1). The unique electronic axis of this system appears to be along the Ni−C bond, as the SOMO appears to be a mixed orbital with significant overlap between the hybridized sp^2 orbital of the coordinating nitrogen on His_{117}, the methyl carbon, and the nickel center (Figure S14). This supports the observed large hyperfine coupling to only one nitrogen atom in the EPR spectra, along with the slightly weaker coupling to the coordinated carbon atom.

The calculated *g*-tensor values and hyperfine coupling constants are generally in agreement with those seen experimentally. Systematic deviation in the form of underestimated *g*-value shifts is commonly seen in DFT calculations owing to overestimated covalency and d−d transition energies and has been noted both for d^9 and d^7 compounds (e.g., Cu^{II}, Co^{II}).[32,33] The hyperfine constants are somewhat overestimated relative to the experimental values (Table 1), though again this is not uncommon in DFT calculations and is highly sensitive to the metal−ligand distances, covalency, and spin−orbit coupling.[32−35]

The TD-DFT results on the Ni^{III}-CH_3 Az species show one dominant transition in the visible region of the spectrum, at 28,606 cm^{-1} (Figure S15); this agrees well with the observed experimental band maximum at 488 nm (~20,500 cm^{-1}). Examining the electronic difference densities shows this band arises from a ligand-to-metal charge-transfer (LMCT) transition, with the primary contribution deriving from the bound methyl group (Figure S15, inset).

Spectroscopic Characterization of Methylated NiAz in the Presence of Excess Reducing Agent Indicates the formation of M121A Ni^{II}-CH_3 Az. *Resonance Raman Spectroscopy Provides Limited Information on M121A Ni-CH_3 Az Intermediates.* Having established the identity of the intermediate species as M121A Ni^{III}-CH_3 Az, we sought to identify the product of the reaction upon decay of the Ni^{III}-CH_3 species. The observation that the M121A Ni^{III}-CH_3 Az intermediate generated using CH_3I accumulates to a much lower extent in the presence of excess reducing agent suggests that the Ni^{III}-CH_3 species can be rapidly reduced, potentially to a Ni^{II}-CH_3 state. While the optical absorption features following the rapid mixing experiments (green trace, Figure 2A) somewhat resemble the starting M121A Ni^{II}Az species, subtle differences in the spectra call into question the identity of this state. The intensity of the band at 416 nm is lower in the product relative to the starting Ni^{II} state, and there are broad, low-intensity features in the near-UV region of the spectrum (300−350 nm). To interrogate the structure of this species, resonance Raman (RR) spectroscopy using 407 nm excitation was used to probe the primary electronic transition. The vibrational signatures are found to be nearly identical for a sample of M121A Ni^{I}Az mixed with CH_3I in the presence of stoichiometric reducing agent and quenched after 5 min when compared to the spectrum of the resting-state, M121A Ni^{II}Az (Figure S16). Both RR profiles show an intense stretch at 343 cm^{-1} that is attributed to the Ni−S bond.[36] This band is strongly enhanced in both samples, indicating that the electronic transition is dominated by S_{Cys}-to-Ni charge-transfer (CT) character. In support of this assignment, the intense band at 764 cm^{-1} is most likely due to the C−S stretching vibration of the cysteine residue, comparable to the band reported for the copper variant.[37] The bands in the 1200−

DOI: 10.1021/acs.inorgchem.8b03546
Inorg. Chem. 2019, 58, 8969−8982

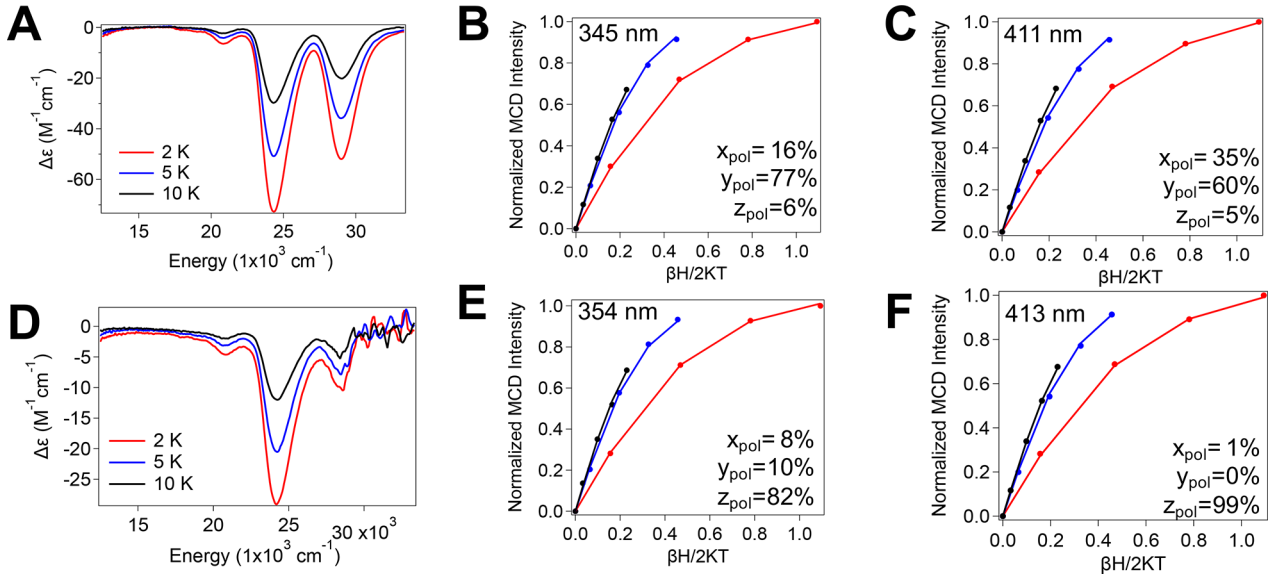

Figure 4. MCD spectra of M121A NiAz. MCD spectra and VTVH curves at 2 K (red), 5 K (blue), and 10 K (black) of (A–C) ∼1 mM M121A Ni^{II}Az and (D–F) ∼1 mM M121A Ni^{I}Az rapidly mixed with 25 mM CH_3I in the presence of 25 mM Ti^{III}(citrate). Samples were prepared in 50 mM phosphate buffer, pH 8.0, containing 50% glycerol. (B, C) VTVH intensities and fitted curves for M121A Ni^{II}Az. $D = -15\ cm^{-1}$, $E/D = 0.206$, $g_x = 2.143$, $g_y = 2.159$, $g_z = 2.171$. (E, F) VTVH intensities and fitted curves for M121A Ni^{II}-CH_3 Az. $D = 8.7\ cm^{-1}$, $E/D = 0.235$, $g_x = 2.09$, $g_y = 2.12$, $g_z = 2.17$. For fitting the VTVH data of both species, the E/D ratios and g-tensor values were taken from the B3LYP calculations (Table S2).

1600 cm^{-1} region can be attributed to histidine stretching modes, which are more enhanced for the M121A NiAz variant than WT NiAz because of the increased active site distortion.[36] However, few changes are seen between the two samples; two bands at 360 and 1500 cm^{-1} reflect the primary differences, though they do not shift when isotopically substituted CH_3I is used and thus likely do not derive from a Ni-CH_3 mode. The lack of an apparent Ni-C mode may be due to either weak enhancement from the probed electronic transition or overlap with pronounced bands from the quartz dewar used in the experimental setup, and ongoing work is aimed at developing strategies to overcome these challenges. EPR experiments indicate that the M121A Ni^{III}-CH_3 state is photolabile at low temperatures (Figure S17), though there is no evidence for photolability of the M121A Ni^{II}-CH_3 Az state.

MCD Spectroscopy Shows M121A Ni^{II}-CH_3 Az Exhibits Distinct Magnetic Properties. Given the limited information gleaned from resonance Raman spectroscopy, more advanced techniques were necessary to identify the species following M121A Ni^{III}-CH_3 Az decay in the presence of excess reducing agent. Magnetic circular dichroism (MCD) spectroscopy is uniquely suited to provide electronic structure information on high-spin Ni^{II} species under aqueous conditions, even for short-lived, trapped intermediates.[38,39] MCD spectra were obtained on the resting M121A Ni^{II}Az state as well as the product of an M121A Ni^{I}Az sample mixed with 10 mM CH_3I in the presence of 25 mM titanium(III) citrate as reducing agent and rapidly frozen. In both samples, the MCD spectra contain three temperature-dependent transitions, therefore exhibiting MCD C-term intensity (Figure 4). The MCD spectra of M121A Ni^{II}Az exhibit two predominant transitions at 345 and 411 nm as well as a weak, broad transition at 480 nm. Similarly, the MCD spectra of the putative M121A Ni^{II}-CH_3 Az species contain two predominant transitions at 354 and 413 nm, each of which is less intense than the corresponding transition in M121A Ni^{II}Az.

A more detailed analysis of the transitions using variable-temperature variable-field (VTVH) measurements, which probe the magnetization saturation behavior of C-term transitions, ultimately revealed that M121A Ni^{II}Az and M121A Ni^{II}-CH_3 Az are in fact two distinct species with different ground-state properties. Resonance Raman investigations on these species have demonstrated that the most intense absorption bands at 411 and 413 nm correspond to $S_{Cys}\rightarrow Ni^{II}$ CT transitions (Figure S16); therefore, these transitions must be polarized along the Ni-S_{Cys} axis.[36] This detail enabled a comparison between experimental data and DFT-calculated zero-field splitting (ZFS) parameters (Table S2), facilitating analysis of the MCD VTVH curves. The DFT-predicted ZFS parameters were used to fit the VTVH data of both M121A Ni^{II}Az and M121A Ni^{II}-CH_3 Az, considering that the 411 and 413 nm transitions, respectively, have to be polarized along the Ni–S_{Cys} bond. We note that the polarizations obtained from the VTVH data are relative to the principal axes of the ZFS tensor; these tensor orientations were taken from the DFT calculations. Using this analysis, only the ZFS parameters obtained from the B3LYP calculations were found to give reasonable results in the initial round of VTVH fits. A hallmark of the B3LYP results is that, while both M121A Ni^{II}Az and M121A Ni^{II}-CH_3 Az are calculated to exhibit large D values, in agreement with SQUID results for WT Ni^{II}Az, the species have *opposite* signs.[40] This can be attributed to the sums of their individual spin–orbit contributions, which are also opposite in sign. After further refinement of D, holding the E/D ratio and the g-values constant at the B3LYP-predicted value, best fits to the data were obtained, delivering D values of $-15\ cm^{-1}$ and $+8.7\ cm^{-1}$ for M121A Ni^{II}Az and M121A Ni^{II}-CH_3 Az, respectively (Figure 4). Moreover, the fits of the VTVH data show that in M121A Ni^{II}Az, the two optical bands at 411 and 345 nm are mostly y-polarized, where, according to the B3LYP calculations, the y-axis of the ZFS tensor aligns with the Ni–S_{Cys} bond (Figures S18–S19). Correspondingly, in M121A Ni^{II}-

DOI: 10.1021/acs.inorgchem.8b03546
Inorg. Chem. 2019, 58, 8969–8982

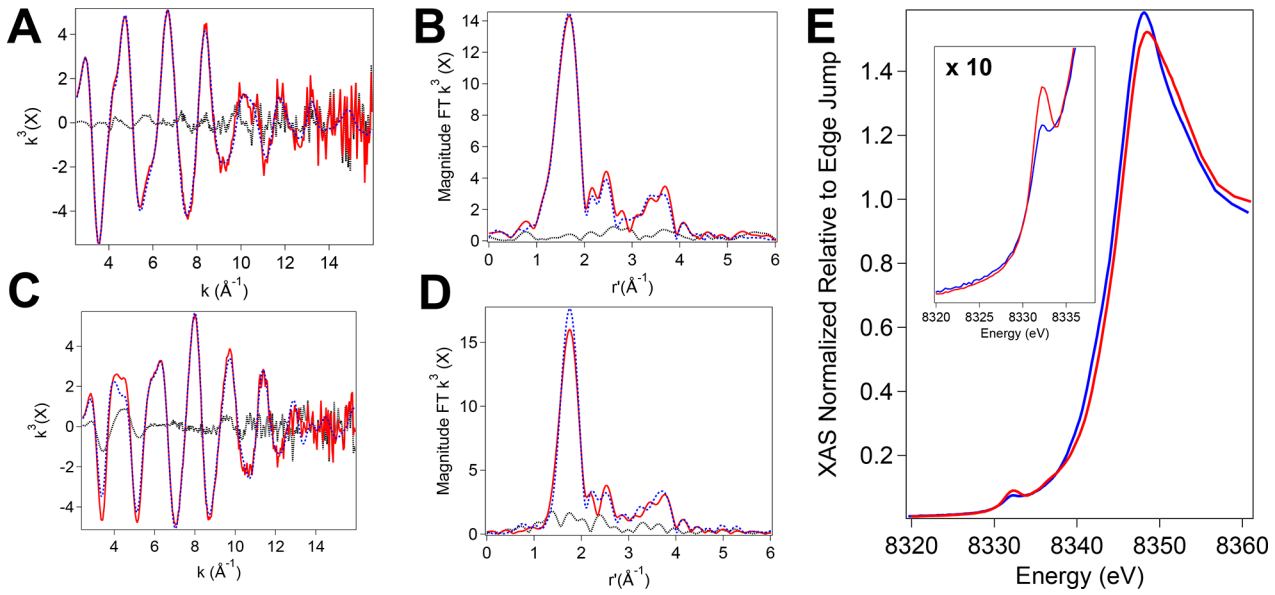

Figure 5. Ni K-edge X-ray absorption data for M121A Ni^{II}Az and M121A Ni^{II}-CH_3 Az. The k^3-weighted EXAFS data of (A) M121A Ni^{II}Az and (C) M121A Ni^{II}-CH_3 Az are depicted with the experimental data (red) overlaid on the best model (blue dashed lines) and the difference spectrum (black dotted traces). The magnitude Fourier transform of the k^3-weighted EXAFS data of (B) M121A Ni^{II}Az and (D) M121A Ni^{II}-CH_3 are depicted with the experimental data (red) overlaid on the best model (blue dashed lines) and the difference spectrum (black dotted traces). (E) The XANES region of the Ni K-edge X-ray absorption spectra of M121A Ni^{II}Az (blue) and M121A Ni^{II}-CH_3 Az (red). (Inset) Pre-edge transitions expanded.

CH_3 Az, the two main optical bands at 413 and 354 nm are *z*-polarized, with the *z*-component of the ZFS tensor pointing along the Ni−S_{Cys} bond (Figures S18−S19). Using the RR assignments as a constraint, the VTVH data indicate a clear difference in the magnetic properties of the ground states of M121A Ni^{II}Az and M121A Ni^{II}-CH_3 Az.

X-ray Spectroscopy Indicates Coordination of an Additional Light Atom to a Ni^{II} Center. To better define the coordination environment about the nickel site of M121A Ni^{II}Az and M121A Ni^{II}-CH_3 Az, nickel K-edge X-ray absorption spectroscopy was employed. The EXAFS regions of the Ni K-edge X-ray absorption spectrum for M121A Ni^{II}Az were best modeled as a three coordinate Ni center with two imidazole ligands at 1.94 Å and a short sulfur ligand at 2.17 Å (Figure 5). Owing to the strong multiple scattering pathways originating from the imidazole ligands, the predicted longer Ni−O interaction originating from the carbonyl oxygen of Gly 45 could not be located. In contrast to the resting M121A Ni^{II}Az state, the EXAFS region of the Ni K-edge X-ray absorption spectrum of M121A Ni^{II}-CH_3 Az is fully consistent with the formation of a 4-coordinate Ni^{II} site with a methyl group bound to nickel. Upon M121A Ni^{II}Az reduction and exposure to CH_3I, a well-ordered carbon scatterer is now modeled at 1.92 Å from the nickel center. The appearance of the Ni-C scatterer is commensurate with the elongation of the two Ni−N (2.02 Å) and one Ni−S (2.24 Å) bond lengths relative to M121A Ni^{II}Az.

The XANES regions of the Ni K-edge X-ray absorption spectra of M121A Ni^{II}Az and M121A Ni^{II}-CH_3 Az are also consistent with the above structural models. The edge positions of both M121A Ni^{II}Az and M121A Ni^{II}-CH_3 Az, at 8339.7(3) and 8440.3(3) eV, are consistent with the Ni^{2+} oxidation state. Both spectra also display a relatively intense pre-edge feature corresponding to a nominal Ni(1s → 3d) transition. Although typically weak, in noncentrosymmetric compounds, the formally dipole-forbidden Ni(1s → 3d) transition can gain intensity through mixing of Ni(4p) character into the wave function of the final state. The intensity of the pre-edge features is thus consistent with both metalloproteins containing Ni^{II} in pseudotetrahedral coordination geometries.[41]

The pre-edge feature observed in the Ni K-edge XANES of M121A Ni^{II}-CH_3 Az is significantly more intense than that observed for M121A Ni^{II}Az. TD-DFT calculations, which reproduce these pre-edge transitions (Figure S20), demonstrate the origin of the observed increase in intensity. For both M121A Ni^{II}Az and M121A Ni^{II}-CH_3 Az, the pre-edge feature is comprised of two nominal Ni(1s → 3d) transitions. The lowest energy transition is into an acceptor state comprised of Ni($3d_{z^2}$) character (dominated by the LUMO), while the next lowest energy transition is into an acceptor state comprised primarily of S($3p_y$)−Ni($3d_{xy}$) antibonding character (dominated by the LUMO+1). Conversion of M121A Ni^{II}Az to Ni^{II}-CH_3 Az does not have a major impact on the degree of Ni(4p) character in the LUMO+1 wave function; elongation of the Ni−S bond causes only a slight decrease in the degree of Ni(4p) composition to the LUMO+1 from 1.7% to 1.4%. However, upon ligation of the $-CH_3$ ligand to the nickel center, the degree of Ni(4p) character in the LUMO increases significantly. The now Ni($3d_{z^2}$)-C(2p) σ^* LUMO of M121A Ni^{II}-CH_3 possesses 3.4% Ni(4p) character relative to <1% Ni(4p) character, contributing to the essentially nonbonding Ni($3d_{z^2}$) LUMO of M121A Ni^{II}Az. This increase in Ni(4p) character results in a significantly more intense pre-edge feature of M121A Ni^{II}-CH_3 Az relative to M121A Ni^{II}Az. Thus, both the XANES and EXAFS regions of the Ni K-edge X-ray absorption spectra of M121A Ni^{II}-CH_3 Az are consistent with the formation of a Ni^{II}-CH_3 moiety at the metalloprotein active site.

Gas Chromatography Analysis Reveals CH_4 to be the Dominant Reaction Product Following CH_3I Addition. Gas chromatography analysis was used to identify and quantify

DOI: 10.1021/acs.inorgchem.8b03546
Inorg. Chem. 2019, 58, 8969−8982

the carbon-based products generated after methyl addition to M121A Ni^{I}Az under a variety of conditions. Using CH_3I as the methyl donor, methane is produced as the primary product (Figure S21). In the absence of a large excess of Eu^{II}DTPA, approximately half an equivalent of CH_4 is observed relative to the initial concentration of M121A Ni^{I}Az. As the residual concentration of Eu^{II}DTPA is increased, methane production also increases, reaching approximately stoichiometric levels; an equivalent change in methane produced by control samples suggests that this increase is simply due to background reactions (Figure S21). Solution pH, time, and concentration of CH_3I added to the solution also affect the amount of methane produced. When the pH is decreased, increasing the effective concentration of free protons in solution, methane production rises, though again to an equivalent extent as is seen in control experiments with $NiSO_4$ (Figure S21). Lower concentrations of added CH_3I also result in substantially lower amounts of CH_4 produced. After approximately 20 min, the optical spectra of the reaction are no longer changing drastically, and production of CH_4 ceases. The formation of methane from a nickel-methyl species generated by CH_3I addition is also observed in model synthetic compounds for ACS.[42] Collectively, these results implicate a persistent interaction of the nickel center with the methyl ligand in the Ni^{II} state. This Ni^{II}-CH_3 Az species is consistent with that characterized using MCD and X-ray spectroscopy.

DISCUSSION

Proposed Reaction Pathways for Methyl Addition to M121A Ni^{I}Az. The work presented here demonstrates that methyl addition to Ni^{I} from methyl iodide occurs via a two-electron, nucleophilic attack on the methyl center, resulting in a transient, low-spin d^7, Ni^{III}-CH_3 species. Within the Az model protein scaffold, this nonporphynoid Ni^{III}-CH_3 state features a distorted trigonal pyramidal or seesaw-like geometry with visible optical bands and a distinct EPR signature that definitively indicates direct coordination of carbon to the nickel center.

However, methyl iodide can react via two-electron methyl cation addition, a radical pathway, or both (Figure 6A). Given that the reaction of M121A Ni^{I}Az with methyl iodide results in the apparent formation of an EPR-active, Ni^{III}-CH_3 species, and reactions using ethyl iodide and ethyl bromide slow formation and accumulation of this intermediate, methyl addition can be said to occur as a carbocation species via nucleophilic attack from the metal center. This contrasts with a radical mechanism, which should generate only the Ni^{II}-CH_3 state and would be expected to proceed more rapidly for the ethyl donors, owing to the increased stability of radicals on long-chain alkanes.[43] The Ni^{III}-CH_3 species formed by nucleophilic addition is relatively long-lived, persisting for minutes at room temperature before decaying into product. The decay pathway of M121A Ni^{III}-CH_3 Az is suggested to occur via a proton-dependent process, evidenced by a KIE of 1.24 for reactions performed in D_2O buffers (Figure 6A). Initially, a hydrolytic decay mechanism was considered; however, neither the recovery of M121A Ni^{I}Az nor the corresponding hydrolysis product, methanol, is detected (Figure S22), leading us to rule out this pathway as a source of Ni^{III}-CH_3 decay. Instead, the detection of CH_4 via gas chromatography suggests that the transient M121A Ni^{III}-CH_3 Az species decays via protonation. This pathway involves direct attack of the methyl group on a solvent-derived proton, similar

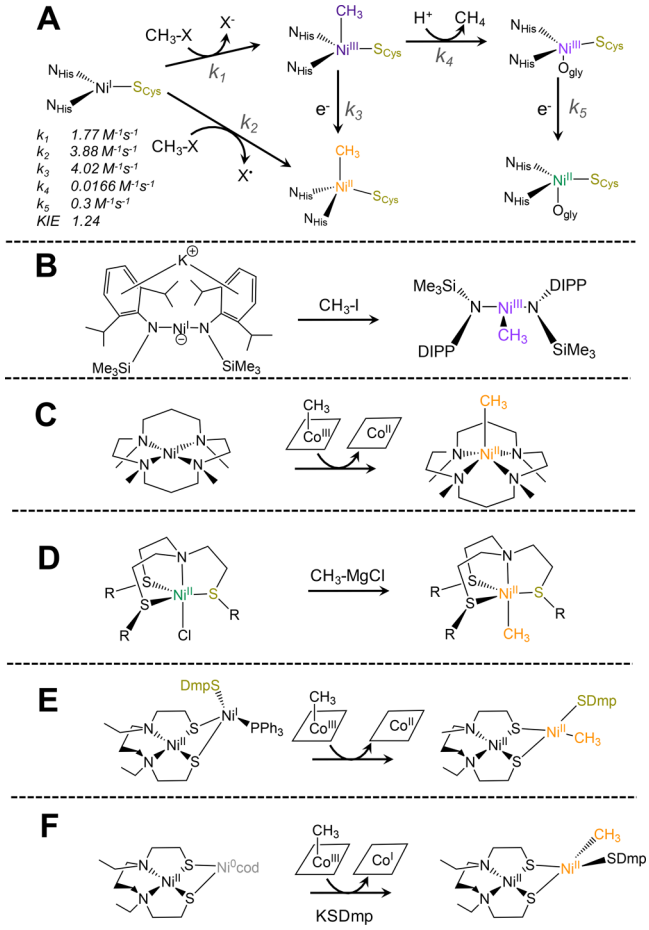

Figure 6. Comparison of methyl addition to nickel systems. (A) Proposed mechanism for addition of CH_3I to M121A Ni^{I}Az. Global kinetic analysis and fitting gives indicated elementary rate constants. (B) Reaction of $K\{Ni[N(SiMe_3)DIPP]_2\}$ with CH_3I via oxidative addition.[56] (C) Reaction of $[Ni^{I}(tmc)]^+$ with $CH_3Co(dmgBF_2)_2L$ to yield Ni^{II}-CH_3 via a radical pathway.[57] (D) Reaction of $[Ni^{II}(NS_3R)$-$Cl]^+$ with CH_3MgCl to form $[Ni^{II}$-$(CH_3)(NS_3R)]^+$.[73] (E) Radical reaction of $Ni^{II}(dadtEt)Ni^{I}(SDmp)(PPh_3)$ with CH_3Co-$(dmgBF_2)_2(Py)$.[59] (F) Reaction of $[Ni^{II}(dadt^{Et})Ni^{0}(cod)]$ with $CH_3Co(dmgBF_2)_2(Py)$ and KSDmp to form Ni^{II}-CH_3.[55]

to early proposed mechanisms for MCR.[44−46] This pathway would result in formation of M121A Ni^{III}Az, which is indeed observed in the EPR spectra to a small extent (≤10%, Figure S23). The resultant, highly oxidizing Ni^{III}Az would then undergo reduction, likely from residual reducing agent in solution, giving the M121A Ni^{II}Az product.

The observation that the M121A Ni^{III}-CH_3 intermediate is formed but accumulates to a much lower extent in the presence of excess reducing agent suggests that the Ni^{III}-CH_3 species can also be directly reduced prior to protonolysis, a process that should be thermodynamically favorable due to the relatively high anticipated reduction potential of a Ni^{III}-CH_3 species. This suggests that a second decay pathway of M121A Ni^{III}-CH_3 Az involves initial reduction to Ni^{II}-CH_3 Az, consistent with evidence provided by MCD and X-ray spectroscopy. An upper bound on the $Ni^{III/II}$-CH_3 Az reduction potential is estimated to be ∼250 mV, as experiments performed in the presence of excess ascorbate show no change in amount of Ni^{III}-CH_3 formed nor the rate of decay (Figure S24).

DOI: 10.1021/acs.inorgchem.8b03546
Inorg. Chem. 2019, 58, 8969−8982

After reduction to Ni^{II}-CH_3 Az, this species can undergo protonation to release methane and form the Ni^{II}Az product. However, stoichiometric or catalytic amounts of methane are not observed, even in the presence of excess Eu^{II}DTPA, indicating that the Ni^{II}-CH_3 state may be stable under anaerobic conditions. Upon exposure to air and exchange of the buffer, the M121A NiAz sample can be recovered and reduced to re-enter the reaction (Figure S25).

Kinetic analysis reveals that the rate of Ni^{I} decay does not directly correlate with the rate of Ni^{III}-CH_3 formation, suggesting that a branched reaction pathway is accessible. This side reaction is attributed to one-electron attack by the metal center to induce homolytic cleavage of CH_3I, generating M121A Ni^{II}-CH_3 Az directly; use of ascorbate as a radical scavenger does not impact the rate of reaction (Figure S24), suggesting spontaneous homolytic degradation of CH_3I prior to metal attack is not a significant contributor to reactivity. SVD and the corresponding amplitude profiles are consistent with this proposal, indicating biphasic formation of a species that is now assigned to the Ni^{II}-CH_3 state (Figure S5). The Ni^{II}-CH_3 species is suggested to form at a slightly faster rate than Ni^{III}-CH_3 from the kinetic modeling, and reduction occurs more rapidly than protonation. Collectively, global analysis of the kinetics and optical spectra support the mechanism and rate constants given in Figure 6 for reactions following CH_3I addition to M121A Ni^{I}Az.

Identification and Characterization of a Biological Ni^{III}-CH_3 Species. Nickel-based catalysts are increasingly used for cross-coupling reactions and carbon-heteroatom bond formation in organic synthesis.[47−49] Often, these catalysts are suggested to proceed through organometallic nickel−carbon bonds in reactions that typically require the nickel center to cycle between the Ni^0/Ni^{II} or Ni^{II}/Ni^{IV} oxidation states.[48,50,51] Conversely, in nature, nickel can accomplish similar chemical reactions but, at this point, is thought to cycle through only three biologically relevant oxidation states: Ni^{I}, Ni^{II}, and Ni^{III}.[12] In low-valent oxidation states, it has been proposed that nickel can form catalytically relevant organometallic intermediates in enzymes pertinent to the carbon cycle, though to date only one biological nickel-alkyl species, featuring nickel coordinated within the MCR hydroporphynoid ring system, has been isolated.[18,21−23] The conjugated F_{430} cofactor of MCR is sterically constrained within the protein and therefore is unable to adopt a highly ruffled conformation.[52] As a result, the Ni^{I} form of F_{430} is thought to feature a four-coordinate nickel center in a square planar geometry with relatively long Ni−N bonds.[52] This nickel coordination environment is distinctly different from that found within ACS.

Conversely, although ACS is also coordinated in a mostly planar geometry, the proximal metal site features a three-coordinate nickel center with coordination to soft cysteinate ligands. This has subtle implications for methyl binding to the metal center, and both the strength of the Ni-C bond and geometry for methyl addition and loss are expected to vary significantly between the ACS and MCR systems. The identification of a four-coordinate Ni^{III}-CH_3 intermediate within azurin thus provides the first relevant model for methyl addition to ACS; notably, no model compounds exist that feature the same coordination number, oxidation, and spin state as those proposed for methylated ACS. Characterization of these methyl-bound intermediates in M121A NiAz provides important metrics for the spectroscopic properties and reactivity that analogous species in native ACS may possess.

The work presented here demonstrates that methyl addition to Ni^{I} from methyl iodide can occur via a two-electron, nucleophilic attack on the methyl center, resulting in a transient, low-spin d^7, Ni^{III}-CH_3 species. Within a biological scaffold, this nonporphynoid Ni^{III}-CH_3 state features a distorted trigonal pyramidal or seesaw-like geometry with visible optical bands and a distinct EPR signature. The M121A NiAz model system offers insight into how the electronic structure of the nickel center contributes to this reactivity, as the Ni^{I}Az state exhibits marked similarity to the reduced, substrate-free A_{red}* state of ACS. However, a Ni^{III}-CH_3 state has never been observed in ACS, potentially owing to the strongly reducing conditions required to carry out the ACS reaction *in vitro*. It is likely that this reducing environment would facilitate rapid reduction from Ni^{III}-CH_3 to Ni^{II}-CH_3, which, as observed here, may be necessary for persistent methylation. A Ni^{III}-CH_3 species is predicted to have a weaker M−C bond than the Co^{III}−CH_3 bond within a base-off corrinoid protein.[53] Therefore, for ACS, it may be that only the presence of a reducing equivalent, either from within the protein or externally donated, can drive the methyl transfer reaction forward. A redox-mediated step provides a means by which to gate reactivity, retaining the methyl group on the cobalt cofactor until an appropriate reduction potential is reached for the reaction to proceed. This could prevent premature methylation of the nickel center, which, in the absence of CO and CoA, may suffer from unproductive protonolysis and release of methane. Furthermore, it appears that a biological Ni^{III}-CH_3 species may have a relatively high reduction potential, as evidenced by rapid reduction of M121A Ni^{III}-CH_3 Az in the presence of even trace amounts of excess reducing agent, complicating efforts to trap a Ni^{III}-CH_3 species within ACS.

Ni^{II}-CH_3 Az May Support Organometallic Reactivity. While both Ni^{II}-CH_3 and Ni^{III}-CH_3 intermediates are formed within the M121A NiAz scaffold, we hypothesize that the Ni^{II}-CH_3 state may be the key intermediate required for further reactivity. The direct formation of Ni^{II}-CH_3 Az via radical addition is similar to generation of traditional synthetic Ni^{II}-CH_3 compounds. These synthetic routes for alkyl-nickel compounds starting from Ni^{I} usually proceed through a radical pathway; two-electron chemistry is generally accomplished from a Ni^0 state,[42,53−55] and only one example exists of the oxidative addition of methyl iodide to Ni^{I}.[56] Alternatively, Ni^{II}-CH_3 species can be generated from a Ni^{II} precursor by the use of anionic methylating agents bound to alkali or alkaline earth metals. This synthetic pathway is completely impractical under aqueous conditions. Relative to synthetic models, the M121A Ni^{I}Az system is unique in that, in addition to undergoing radical methyl addition, the two-electron, nucleophilic addition of a cationic methyl group is accessible. This is the pathway that has been proposed for native ACS.

Further differentiation between M121A Ni^{I}Az and synthetic models is found in the primary coordination sphere. Like ACS, prior to substrate binding, M121A Ni^{I}Az contains a 3-coordinate, trigonal planar ligand system featuring a directly coordinated thiolate ligand (Figure 6A). Most of the ACS model compounds feature square-planar, 4-coordinate nickel centers bound to either amine (e.g., 1,4,8,11-tetramethyl-1,4,8,11-tetra-azacyclotetradecane, tmc),[57] thioether, or phosphine (e.g., 1,2-bis(diphenylphosphino)ethane, dppe) ligands (Figure 6B−E).[54,58] These nonbiological ligand scaffolds and geometries will modulate the strength of the Ni−CH_3 bond

DOI: 10.1021/acs.inorgchem.8b03546
Inorg. Chem. 2019, 58, 8969−8982

and, consequently, further reactions with CO. Therefore, we must instead examine the reactivity of a 4-coordinate Ni^{II}-CH_3 system, which more closely resembles the structure of ACS. Tatsumi has developed a dinuclear $Ni^{II}Ni^{I}$ compound featuring a 4-coordinate Ni^{I} center with 2,6-dimesitylphenylthiolate ($dmpS^-$) and triphenylphosphine ligands; however, significant spectral differences between this model compound and the reduced states of ACS are suggested to arise because of differences in the coordination environment.[59] Methyl addition to this compound results in a square planar complex (Figure 6E), with subsequent degradation upon exposure to CO.[59] The distorted trigonal pyramidal Ni^{II}-CH_3 species formed within the M121A NiAz environment and the constraints of a large, macromolecular ligand framework thus provide a more appropriate platform to pursue reactivity similar to that seen in the ACS enzyme.

Resonance Raman experiments demonstrate that the Ni–S_{Cys} electronic transition dominates the resonance Raman profile in the low-frequency region (Figure S16), not unlike what is reported for the Cu–S_{cys} M121A variant.[37] Czernuszewicz *et. al* attributes the strong enhancement of bands at 363 and 763 cm^{-1} to the coupling between Cu–S_{cys} and internal ligand deformation modes; a comparable degree of coupling is anticipated in the nickel variant of the system. Using the knowledge that the key CT transition lies along this Ni–S axis, MCD spectroscopy was used to provide a complementary probe of the electronic structure of these integer spin systems.[60−63] The VTVH MCD spectra of M121A Ni^{II}Az and M121A Ni^{II}-CH_3 Az identify the latter species as a distinct, high-spin Ni^{II}-CH_3 state that shows similar $S(\pi) \rightarrow Ni$ LMCT transitions as M121A Ni^{II}Az but is clearly distinct with respect to the magnetic properties of the ground state (where the *D* values have opposite signs). Interestingly, the magnitude of the *D* value is similar to that previously reported for a high-spin Ni^{II}-CH_3 compound featuring four-fold symmetry.[53,64]

Analysis of the MO diagrams of M121A Ni^{II}Az and M121A Ni^{II}-CH_3 Az can be used for further interrogation of the electronic structure. Because the Ni^{II} center has a high-spin, d^8 electron configuration, all majority (α-) spin d-orbitals are fully occupied. Consequently, all spin-allowed d–d and CT transitions occur within the minority (β-) spin manifold (Figure 7). Remarkably, in M121A Ni^{II}Az, the $S(\pi)$ thiolate donor orbital forms a π-bond with the empty Ni β-d_{xy} orbital, emphasizing how the active site is primed to enforce a strong metal–sulfur π-interaction instead of a σ-interaction. The β-HOMO corresponds to the bonding combination between these orbitals (Figure 7). Correspondingly, the CT transitions observed by optical spectroscopy are of $S(\pi) \rightarrow Ni(d)$ type. In addition, the β-MO diagram (Figure S26) indicates that M121A Ni^{II}Az has occupied d_{yz}, $d_{x^2-y^2}$, and d_{xz} orbitals (in decreasing energy, respectively).

Upon coordination of the methyl group, the CH_3 ligand forms a new σ-bond with the empty Ni β-d_{z^2} orbital. The energy ordering of the occupied β-d orbitals of Ni is inverted for M121A Ni^{II}-CH_3 Az, with the $d_{x^2-y^2}$, d_{xz}, and d_{yz} orbitals occupied in decreasing energy. Additionally, in the methyl intermediate, the occupied β-d orbitals are much lower in energy and closer to the β-HOMO level when compared to M121A Ni^{II}Az (Figure S26). This is likely due to a decrease in the effective nuclear charge of the Ni center in the presence of the strongly donating methyl ligand. The difference in the sign of *D* originates directly from the SOC contribution, which differs between M121A Ni^{II}Az and M121A Ni^{II}-CH_3 Az due to

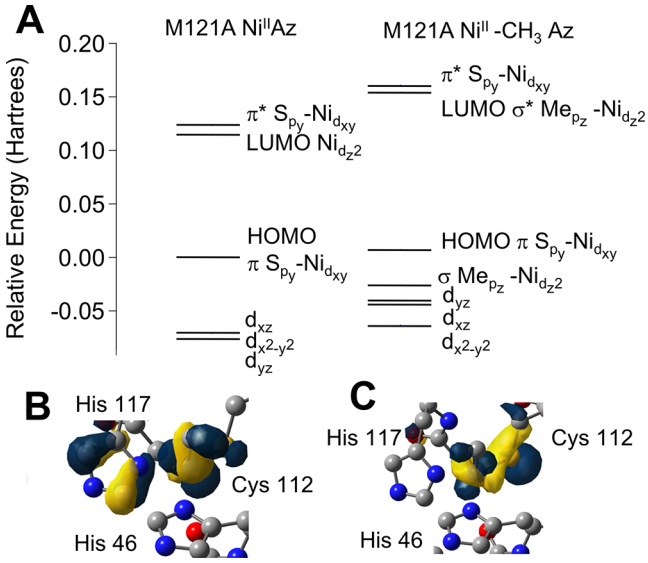

Figure 7. Frontier molecular orbitals. (A) Relative β-spin frontier molecular orbital diagram of M121A Ni^{II}Az and M121A Ni^{II}-CH_3 Az obtained from B3LYP/def2-TZVP calculations. (B) Contour plot of the β-d_{xz} orbital from M121A Ni^{II}-CH_3 Az. (C) Contour plot of the β-d_{yz} orbital from M121A Ni^{II}-CH_3 Az.

the discussed differences in d-orbital sequence and relative energies. Other contributions to *D* are negligible. Interestingly, the low-lying, occupied β-d_{xz} and β-d_{yz} orbitals in M121A Ni^{II}-CH_3 Az point into the empty space trans to the His_{117} residue, providing a binding site for an incoming CO ligand. Here, the CO(π^*) orbitals would be able to form significantly stronger π-backbonding interactions with the β-d_{xz} and β-d_{yz} orbitals of M121A Ni^{II}-CH_3 Az relative to M121A Ni^{II}Az. Hence, whereas the latter species does not interact with CO (Figure S27), these results suggest that CO may be able to form a transient CO complex with the Ni^{II}-CH_3 intermediate, prior to possible insertion into the Ni^{II}-CH_3 bond.

The potential for CO binding to the Ni^{II}-CH_3 state was explored through preliminary time-resolved optical studies. A population of M121A Ni^{II}-CH_3 Az was generated by mixing CH_3I into M121A Ni^{I}Az in the presence of excess reducing agent, conditions that were designed to mimic those used for preparation of the MCD and XAS samples. Upon injection of CO-saturated buffer, the signals attributed to M121A Ni^{II}-CH_3 quickly decayed, at a rate substantially higher than that seen in corresponding control experiments (Figure S28). While the product(s) from this experiment remain unresolved and a comprehensive investigation is beyond the scope of this work and will form the body of a subsequent publication, the rapid quenching of the M121A Ni^{II}-CH_3 species by CO addition suggests great potential for downstream reactivity to be installed and characterized within the NiAz model protein system.

Implications for the Role of Nickel-Methyl Species in the ACS Catalytic Cycles. The ability of M121A NiAz to form both a Ni^{III}-CH_3 and Ni^{II}-CH_3 species provides an opportunity to explore reactions within the context of both MCR and ACS catalysis. The lack of hydrolysis observed in either oxidation state is consistent with the reactivity seen in MCR, in which the reactive methyl species generated from methyl-CoM solely reacts to form methane. In organisms capable of methanol production or activation, the cobalt

DOI: 10.1021/acs.inorgchem.8b03546
Inorg. Chem. 2019, 58, 8969–8982

corrinoid-containing MtaABC complex is used instead of nickel-containing MCR.[65−67] Hydrolysis of the methyl-bound state of ACS to generate methanol has also never been detected. The methylated species is suggested to be sufficiently stable to be isolated in the absence of added CO, though this is only implied by subsequent reactivity to generate acetyl-CoA and characterization of a Ni^{II}-CH_3 state remains elusive. Interestingly, minor amounts of methane have been observed as a side metabolic product of acetogenic bacteria, though to such a small extent that this cannot be a dominant decay pathway of methylated ACS. Thus, there must be additional electronic or structural influences within the ACS active site to prevent protonolysis.

The isolation of distinct Ni-CH_3 species within Az offers exploration of the molecular requirements for subsequent CO binding. It has been proposed that substrate binding in ACS can occur via random ordering.[13] However, we hypothesize that CO will be unable to bind to an electron-deficient Ni^{III}-CH_3 center. Moreover, electronic structure analysis shows that the resulting structure of the Ni^{II}-CH_3 species following methyl binding induces a shift of the occupied β-d_{xz} and β-d_{yz} orbitals to lower energy, priming them for interaction with an incoming CO ligand. This indicates that the formation of a Ni^{II}-CH_3 species may be necessary for CO binding, and that, in turn, formation of a (potentially transient) CO adduct is a prerequisite for formation of an acetyl group.

Additionally, the requirement of a redox-active buffer or low-potential conditions for ACS activity supports the idea of rapid reduction to a Ni^{II}-CH_3 state following methylation of the Ni_P site but prior to CO binding.[68−70] While the [4Fe-4S] cluster has been suggested to be redox-inactive for *in vitro* ACS turnover due to sluggish measured ET kinetics,[16] we postulate that, *in vivo*, conformational changes may permit an electron to reversibly derive from the [4Fe-4S] cluster, another redox-active site in the protein, or even the Ni_D site. This second nickel center should have a $Ni^{III/II}$ couple that occurs at a lower potential than the Ni_P^{III}-CH_3 site owing to the bisamidinate ligation.[71] Like the reactivity seen here for M121A NiAz, although the methyl group adds to ACS from the CoFeSP protein in a two-electron process, an internal electron-transfer step could rapidly reduce the transiently formed Ni^{III}-CH_3 to Ni^{II}-CH_3, enabling CO binding and subsequent insertion into the Ni-CH_3 bond.[55,69,72,73] Importantly, we suggest that this redox event may act as a gate for reactivity, transferring the methyl group only when a specific potential is reached. Acyl transfer to CoA would allow release of that electron from the Ni_P site, potentially back to the [4Fe-4S] cluster or the Ni_D center, and regeneration of the Ni^I state. The ability to access this type of reactivity in the M121A Ni^IAz model system, which has well-defined oxidation states within a simple active site, is currently being explored in our lab and will likely shed important insight into the order of substrate binding and reactions in native ACS.

CONCLUSIONS

Methyl binding to a protein-based model of acetyl-CoA synthase, the M121A mutant of nickel-substituted azurin, can occur via nucleophilic addition to the Ni^I oxidation state. Using methyl iodide, a transient Ni^{III}-CH_3 intermediate is generated, which has been characterized using optical and EPR spectroscopy in conjunction with DFT calculations. The Ni^{III}-CH_3 intermediate is rapidly reduced to a Ni^{II}-CH_3 species, which has been characterized using MCD and X-ray spectroscopy to support the coordination of a carbon atom to the nickel center. The reaction mechanism has been quantitatively modeled using global kinetic simulations coupled with singular value decomposition analysis. M121A Ni^{III}-CH_3 Az represents the first well-defined Ni^{III}-CH_3 species within a distorted trigonal pyramidal environment, and its characterization within a biologically derived system is of great relevance for understanding the reaction mechanism of ACS. Additionally, the ability to isolate both an EPR-active Ni^{III}-CH_3 state and an MCD-active Ni^{II}-CH_3 species provides a platform for further investigation of the reactivity requirements for both ACS and MCR enzyme systems. Overall, the metal−alkyl species characterized within the M121A NiAz system serve as models for the bioorganometallic catalytic intermediates found in multiple nickel enzymes. Ongoing efforts are aimed at characterizing potential reactivity of the methylated species upon introduction of additional ACS substrates, including CO.

MATERIALS AND METHODS

Solutions were prepared using deionized water (18.2 MOhm, Elga Technologies) unless otherwise noted. Reagents were purchased from Sigma-Aldrich, Alfa Aesar, or VWR Technologies, unless otherwise noted. D_2O was obtained from Cambridge Isotopes.

Optical Absorption Spectroscopy. All absorption spectra were measured on either a Shimadzu UV-2600 spectrophotometer or a Cary 60 spectrophotometer using septa-capped cuvettes. For rapid mixing experiments with methyl iodide (Sigma-Aldrich), a 50 mM or 100 mM stock suspension of CH_3I was prepared in 50 mM phosphate buffer anaerobically inside a septum-capped vial. Due to low solubility and potential instability of CH_3I in water, a fresh suspension of CH_3I was prepared immediately prior to each experiment. Using a gastight syringe (Hamilton), aliquots of the CH_3I suspension were hand-mixed into a septum-capped cuvette containing M121A Ni^IAz and placed within the spectrophotometer within 10 s. Spectra were collected from 700 to 240 nm every 35 s over 48 min using a 0.2 cm path length and baseline-corrected using Igor Pro (Wavemetrics, Lake Oswego, OR). For experiments using both CH_3I and CO, CO-saturated buffer was prepared in 50 mM phosphate buffer and added to a final concentration of 0.22 mM ∼ 3 min after M121A Ni^IAz reacted with 1.1 mM of CH_3I.

Kinetic Modeling. Singular value decomposition (SVD) analysis and kinetic simulations were accomplished using the KinTek software (version 7.2) with FitSpace Explorer and SpectraFit.[74,75] Baseline-corrected UV−vis data were imported to KinTek, and SVD analysis performed to decompose the absorbance spectra and isolate the representative spectral features of each component contributing to the overall absorbance. The SVD components were fit to the following proposed kinetic model. Best-fit rate constants in H_2O are given in Figure 6.

$$\text{M121A } Ni^{I}\text{Az} + CH_3I \xrightarrow{k_1} \text{M121A } Ni^{III}CH_3\text{Az} \quad (1)$$

$$\text{M121A } Ni^{I}\text{Az} + CH_3I \xrightarrow{k_2} \text{M121A } Ni^{II}CH_3\text{Az} \quad (2)$$

$$\text{M121A } Ni^{III}CH_3\text{Az} + e^- \xrightarrow{k_3} \text{M121A } Ni^{II}CH_3\text{Az} \quad (3)$$

$$\text{M121A } Ni^{III}CH_3\text{Az} + H^+ \xrightarrow{k_4} \text{M121A } Ni^{III}\text{Az} + CH_4 \quad (4)$$

$$\text{M121A } Ni^{III}\text{Az} + e^- \xrightarrow{k_5} \text{M121A } Ni^{II}\text{Az} \quad (5)$$

The concentrations could vary in the simulations by <10% to account for errors in estimated extinction coefficients and syringe error.

Electron Paramagnetic Resonance Spectroscopy. Continuous-wave X-band EPR measurements were collected at either 100 K on a Bruker EMXPlus equipped with a Bruker variable-temperature unit or at 30 K using a liquid helium cryostat using a Bruker EMX instrument equipped with an Oxford flow cryostat (ITC-500). An

DOI: 10.1021/acs.inorgchem.8b03546
Inorg. Chem. 2019, 58, 8969−8982

aliquot of CH_3I, $^{13}CH_3I$ (Sigma-Aldrich), or CD_3I (Sigma-Aldrich) was rapidly hand-mixed into a septum-capped EPR tube (Wilmad Lab glass, 727-SQ-250MM) containing 300 μM M121A Ni^{I}Az to a final concentration of 1.5 mM and quenched at varying time points in a liquid nitrogen-isopentane bath held at approximately 150 K. Spectra were collected at 30 K with a modulation frequency of 100 kHz and a modulation amplitude of 10 G at a power of 0.2 mW using 30 dB attenuation. For high-resolution spectra at 100 K, a modulation amplitude of 1 G was used, and data points were collected every 0.1 G with a time constant of 10.24 ms and a conversion time of 40 ms. Photolysis studies employed the use of a white LED light (Luxeon). A power saturation study of the trapped intermediate was collected at 5 K at the Ohio Advanced EPR Facility at Miami University. Spectra were baseline-corrected by subtraction of a spline using Igor Pro (Wavemetrics, Lake Oswego, OR) data analysis software. The baseline-corrected EPR spectra were simulated with the EasySpin toolbox[76] within MATLAB.

Magnetic Circular Dichroism (MCD) Spectroscopy. Samples for MCD spectroscopy were prepared anaerobically inside of a glovebox. M121A Ni^{II}Az was diluted to a final concentration of 1 mM in 50 mM phosphate buffer, pH 8.0, containing 50% glycerol. This sample was loaded into a custom-made MCD cell and flash frozen in liquid nitrogen to generate an optical glass. Next, M121A Ni^{I}Az was prepared by reducing ~2 mM of M121A Ni^{II}Az with 25 mM titanium(III) citrate (Ti^{III}Cit). The reduced protein sample was diluted with glycerol to produce a 50% glycerol sample that would generate an optical glass upon rapid freezing. A solution of CH_3I was prepared in 50 mM phosphate buffer, and 50 mM of CH_3I was rapidly mixed into the protein-containing glycerol solution. After reacting for 20 min to account for the slowed kinetics in glycerol (Figure S29), the M121A Ni^{I}Az + CH_3I product sample containing excess reductant was loaded into a custom-made MCD cell, brought out of the glovebox in a sealed vial, and flash frozen in liquid nitrogen to generate an optical glass.

The MCD setup employs an Oxford SM4000 cryostat and a JASCO J-815 CD spectrometer. The SM4000 cryostat consists of a liquid helium-cooled superconducting magnet providing horizontal magnetic fields of 0−7 T. The J-815 spectrometer uses a gaseous nitrogen-cooled xenon lamp and a detector system consisting of two interchangeable photomultiplier tubes in the UV−vis and NIR range. The samples were loaded into a 1.5−300 K variable-temperature insert, which offers optical access to the sample via four optical windows made from Suprasil B quartz. The MCD spectra were measured in [θ] = mdeg and converted into MCD extinction coefficients, $\Delta\varepsilon$ [M^{-1} cm^{-1} T^{-1}], using the conversion factor $\Delta\varepsilon = \theta/(32{,}980 \times c \times d \times B)$, where c is the concentration, B is the magnetic field, and d is the path length. The product $c \times d$ can be substituted by $A_{MCD}/\varepsilon_{UV-vis}$, where A is the absorbance of the sample measured by the CD spectrometer, and ε_{UV-vis} is the extinction coefficient from UV−vis.[77,78] The spectra were recorded at different temperatures (2, 5, and 10 K) and magnetic fields (0, 1, 3, 5, and 7 T). Experiments were conducted by varying the field at the respective temperatures.

The theoretical background for MCD spectroscopy was developed by Stephens et al. and has been summarized in several reviews and articles.[62,77−83] MCD spectroscopy is governed by eq 6, where I is the MCD intensity, T is the temperature, B is the magnetic field, and the function $f(E)$ represents the band shape of an absorption band:

$$I \sim \left[A_1\left(\frac{-\partial f(E)}{\partial E}\right) + \left(B_0 + \frac{C_0}{kT}\right)f(E)\right] \times B \tag{6}$$

The VTVH data were fitted using the general method developed by Neese and Solomon.[79] The analysis of the C-term intensity can be fitted based on the following eq 7:

$$\frac{\Delta\varepsilon}{E} = \frac{\gamma}{4 \times \pi \times S}\int_0^{\pi}\int_0^{2\pi}\sum_i N_i(l_x\langle S_x\rangle M_{yz}^{eff} + l_y\langle S_y\rangle M_{xz}^{eff} + l_z\langle S_z\rangle M_{xy}^{eff})\sin(\theta)d\theta d\phi \tag{7}$$

where the sum over i runs over the sublevels of the ground state, $\Delta\varepsilon/E$ is the MCD intensity, M^{eff} are the effective transition dipole moment products, l_i are the angles between the magnetic field axes and the molecular coordinate system, N_i are the Boltzmann populations, $\langle S_i\rangle$ are the spin-expectation values, γ is a constant, and S is the total spin. The individual polarizations of the MCD bands can then be calculated using M^{eff} values obtained from the fit of the VTVH saturation curves using eq 8:

$$\%x = 100 \times \frac{(M_{xz}^{eff} \times M_{xy}^{eff})^2}{(M_{xz}^{eff} \times M_{xy}^{eff})^2 + (M_{xz}^{eff} \times M_{yz}^{eff})^2 + (M_{yz}^{eff} \times M_{xy}^{eff})^2} \tag{8}$$

To limit the number of variables and provide a starting point for the fitting of the VTVH data, zero-field splitting (ZFS) parameters were first obtained through DFT calculations. Next, the DFT-predicted ZFS parameters were used to fit the VTVH data of both M121A Ni^{II}Az and M121A Ni^{II}-CH_3 Az, keeping in mind that the polarization was constrained to lie along the Ni−S(Cys) bond.

Ni K-Edge X-ray Absorption Spectroscopy. Samples for X-ray spectroscopy were prepared anaerobically inside of a glovebox. Samples contained a final concentration of ~1 mM M121A Ni^{I}Az with 25 mM titanium(III) citrate (Ti^{III}Cit). The reduced protein sample was diluted with glycerol to produce a 50% glycerol sample. Samples were reacted with 20 mM CH_3I, and the reaction allowed to proceed for ~5 min prior to freezing. Samples were loaded into aluminum sample holders between Kapton tape windows and quickly frozen in liquid nitrogen. Data were collected on the HXMA beamline (06ID-1) at the Canadian Light Source (Saskatoon, Saskatchewan, Canada) with samples maintained at 15 K throughout data collection with the use of an Oxford Instruments He(l) flow cryostat. A Si(220) double monochromator, which was detuned 40% for harmonic rejection, was used for light monochromatization. The beam (1 × 1 mm spot size) was moved after every other scan to avoid photodamage of the sample. Fluorescence data were collected with a 30-element solid-state Ge detector array (Canberra Industries) with total count rates kept under 35 kHz with a 3 μm cobalt metal filter placed between the sample and the detector. Energy calibrations were performed by simultaneously recording the spectrum of Ni foil (first inflection point set to 8333.0 eV). Data were collected in 5 eV steps from 8133−8313 eV (1 s integration time), 0.3 eV steps from 8313−8363 eV (3 s integration time), 2 eV steps from 8363−8633 eV (5 s integration time), and 5 eV steps from 8633 eV − k = 16 $Å^{-1}$ (5 s integration time). A total of 10 individual data sets were combined for each spectrum; individual channels of each data set were inspected prior to data averaging. Data workup and analysis was performed as previously described using EXAFS123 as previously described on unfiltered $k^3(\chi)$ data refined over the range of k = 2.5−15.5 $Å^{-1}$.[84] Alternative fits with statistics are presented in the Supporting Information (Tables S3−S4).

■ ASSOCIATED CONTENT

Supporting Information

The Supporting Information is available free of charge on the ACS Publications website at DOI: 10.1021/acs.inorgchem.8b03546.

Detailed materials and methods as well as supplemental optical titrations, EPR spectra and simulations, MCD molecular orbital diagrams, statistically significant alternative EXAFS fits, XANES spectra and TD-DFT calculations, DFT structures, coordinates, and a sample input file (PDF)

■ AUTHOR INFORMATION

Corresponding Author

*E-mail: shafaat.1@osu.edu.

DOI: 10.1021/acs.inorgchem.8b03546
Inorg. Chem. 2019, 58, 8969−8982

ORCID

Anastasia C. Manesis: 0000-0001-7162-3676
Jason Shearer: 0000-0001-7469-7304
Nicolai Lehnert: 0000-0002-5221-5498
Hannah S. Shafaat: 0000-0003-0793-4650

Funding

This work has been supported by the OSU Department of Chemistry and Biochemistry, an ACS PRF grant (57403-DNI6) to H.S.S., an award from the Department of Energy Early Career Research Program (EC DE-SC0018020) to H.S.S., an NSF grant (CHE-1565766) to J.S., and an NIH award (GM120641) to J.S. Research described in this paper was performed at the Canadian Light Source at the HXMA beamline (06ID-1), which is supported by the Canada Foundation for Innovation, Natural Sciences and Engineering Research Council of Canada, the University of Saskatchewan, the Government of Saskatchewan, Western Economic Diversification Canada, the National Research Council Canada, and the Canadian Institutes of Health Research.

Notes

The authors declare no competing financial interest.

■ ACKNOWLEDGMENTS

We gratefully acknowledge Professor Yi Lu for providing starting pET9a M121A plasmid, Professor David Grahame for the generous gift of methylco(III)binamide, Professor Stephen Ragsdale for insightful conversations, Dr. Robert McCarrick at the Ohio Advanced EPR Facility at Miami University for assistance with EPR, Sean Marguet for helpful discussions, Camille Schneider for help with GC calibrations, and Ayla Robinson for initial help with experiments.

■ REFERENCES

(1) Ragsdale, S. W. Nickel and the Carbon Cycle. *J. Inorg. Biochem.* **2007**, *101* (11−12), 1657−1666.

(2) Grahame, D. A. Acetate C-C Bond Formation and Decomposition in the Anaerobic World: The Structure of a Central Enzyme and Its Key Active-Site Metal Cluster. *Trends Biochem. Sci.* **2003**, *28* (5), 221−224.

(3) Bender, G.; Pierce, E.; Hill, J. A.; Darty, J. E.; Ragsdale, S. W. Metal Centers in the Anaerobic Microbial Metabolism of CO and CO2. *Metallomics* **2011**, *3* (8), 797−815.

(4) Huber, C.; Wächtershäuser, G. Peptides by Activation of Amino Acids with CO on (Ni,Fe)S Surfaces: Implications for the Origin of Life. *Science* **1998**, *281* (5377), 670−672.

(5) Russell, M. J.; Martin, W. The Rocky Roots of the Acetyl-CoA Pathway. *Trends Biochem. Sci.* **2004**, *29* (7), 358−363.

(6) Wächtershäuser, G. Evolution of the First Metabolic Cycles. *Proc. Natl. Acad. Sci. U. S. A.* **1990**, *87* (1), 200−204.

(7) Brack, A. *The Molecular Origins of Life: Assembling Pieces of the Puzzle*; Cambridge University Press: Cambridge, UK, 1998.

(8) Glass, J. B.; Dupont, C. L. Oceanic Nickel Biogeochemistry and the Evolution of Nickel Use. *The Biological Chemistry of Nickel*; Royal Society of Chemistry: Cambridge, UK, 2017; Chapter 2.

(9) Ragsdale, S. W. Biochemistry of Methyl-Coenzyme M Reductase: The Nickel Metalloenzyme That Catalyzes the Final Step in Synthesis and the First Step in Anaerobic Oxidation of the Greenhouse Gas Methane. *The Metal-Driven Biogeochemistry of Gaseous Compounds in the Environment*; Springer: Dordrecht, 2014; Vol. *14*, pp 125−145.

(10) Boer, J. L.; Mulrooney, S. B.; Hausinger, R. P. Nickel-Dependent Metalloenzymes. *Arch. Biochem. Biophys.* **2014**, *544*, 142−152.

(11) Ragsdale, S. W. Nickel-Based Enzyme Systems. *J. Biol. Chem.* **2009**, *284* (28), 18571−18575.

(12) Can, M.; Armstrong, F. A.; Ragsdale, S. W. Structure, Function, and Mechanism of the Nickel Metalloenzymes, CO Dehydrogenase, and Acetyl-CoA Synthase. *Chem. Rev.* **2014**, *114* (8), 4149−4174.

(13) Seravalli, J.; Ragsdale, S. W. Pulse-Chase Studies of the Synthesis of Acetyl-CoA by Carbon Monoxide Dehydrogenase/Acetyl-CoA Synthase: Evidence for a Random Mechanism of Methyl and Carbonyl Addition. *J. Biol. Chem.* **2008**, *283* (13), 8384−8394.

(14) Can, M.; Giles, L. J.; Ragsdale, S. W.; Sarangi, R. X-Ray Absorption Spectroscopy Reveals an Organometallic Ni-C Bond in the CO-Treated Form of Acetyl-CoA Synthase. *Biochemistry* **2017**, *56* (9), 1248−1260.

(15) George, S. J.; Seravalli, J.; Ragsdale, S. W. EPR and Infrared Spectroscopic Evidence That a Kinetically Competent Paramagnetic Intermediate Is Formed When Acetyl-Coenzyme A Synthase Reacts with CO. *J. Am. Chem. Soc.* **2005**, *127* (39), 13500−13501.

(16) Bramlett, M. R.; Stubna, A.; Tan, X.; Surovtsev, I. V.; Münck, E.; Lindahl, P. A. Mössbauer and EPR Study of Recombinant Acetyl-CoA Synthase from Moorella Thermoacetica. *Biochemistry* **2006**, *45* (28), 8674−8685.

(17) Lindahl, P. A. Acetyl-Coenzyme A Synthase: The Case for a Nip 0-Based Mechanism of Catalysis. *JBIC, J. Biol. Inorg. Chem.* **2004**, *9* (5), 516−524.

(18) Yang, N.; Reiher, M.; Wang, M.; Harmer, J.; Duin, E. C. Formation of a Nickel−Methyl Species in Methyl-Coenzyme M Reductase, an Enzyme Catalyzing Methane Formation. *J. Am. Chem. Soc.* **2007**, *129* (36), 11028−11029.

(19) Dey, M.; Telser, J.; Kunz, R. C.; Lees, N. S.; Ragsdale, S. W.; Hoffman, B. M. Biochemical and Spectroscopic Studies of the Electronic Structure and Reactivity of a Methyl−Ni Species Formed on Methyl-Coenzyme M Reductase. *J. Am. Chem. Soc.* **2007**, *129* (36), 11030−11032.

(20) Dey, M.; Li, X.; Zhou, Y.; Ragsdale, S. W.Evidence for Organometallic Intermediates in Bacterial Methane Formation Involving the Nickel Coenzyme F430*Organometallics in Environment and Toxicology: Metal Ions in Life Sciences*; Royal Society of Chemistry: Cambridge, UK, 2010; pp 71−110.

(21) Cedervall, P. E.; Dey, M.; Li, X.; Sarangi, R.; Hedman, B.; Ragsdale, S. W.; Wilmot, C. M. Structural Analysis of a Ni-Methyl Species in Methyl-Coenzyme M Reductase from Methanothermobacter Marburgensis. *J. Am. Chem. Soc.* **2011**, *133* (15), 5626−5628.

(22) Sarangi, R.; Dey, M.; Ragsdale, S. W. Geometric and Electronic Structures of the NiI and Methyl−NiIII Intermediates of Methyl-Coenzyme M Reductase. *Biochemistry* **2009**, *48* (14), 3146−3156.

(23) Mahlert, F.; Bauer, C.; Jaun, B.; Thauer, R. K.; Duin, E. C. The Nickel Enzyme Methyl-Coenzyme M Reductase from Methanogenic Archaea: In Vitro Induction of the Nickel-Based MCR-Ox EPR Signals from MCR-Red2. *JBIC, J. Biol. Inorg. Chem.* **2002**, *7* (4−5), 500−513.

(24) Mahlert, F.; Grabarse, W.; Kahnt, J.; Thauer, R. K.; Duin, E. C. The Nickel Enzyme Methyl-Coenzyme M Reductase from Methanogenic Archaea: In Vitro Interconversions among the EPR Detectable MCR-Red1 and MCR-Red2 States. *JBIC, J. Biol. Inorg. Chem.* **2002**, *7* (1−2), 101−112.

(25) Manesis, A. C.; O'Connor, M. J.; Schneider, C. R.; Shafaat, H. S. Multielectron Chemistry within a Model Nickel Metalloprotein: Mechanistic Implications for Acetyl-CoA Synthase. *J. Am. Chem. Soc.* **2017**, *139* (30), 10328−10338.

(26) Guthrie, J. P. Hydrolysis of Esters of Oxy Acids: PKa Values for Strong Acids; Brønsted Relationship for Attack of Water at Methyl; Free Energies of Hydrolysis of Esters of Oxy Acids; and a Linear Relationship between Free Energy of Hydrolysis and PKa Holding over a Range of 20 PK Units. *Can. J. Chem.* **1978**, *56* (17), 2342−2354.

(27) Alder, R. W.; Phillips, J. G. E.; Huang, L.; Huang, X. *Encyclopedia of Reagents for Organic Synthesis*; John Wiley & Sons: New York, 2005.

(28) Gore, E. S.; Busch, D. H. Stable Octahedral, Low-Spin Nickel(III) Complexes of a Tetradentate Macrocyclic Ligand Having Saturated Nitrogen Donors. *Inorg. Chem.* **1973**, *12* (1), 1−3.

DOI: 10.1021/acs.inorgchem.8b03546
Inorg. Chem. 2019, 58, 8969−8982

(29) Ragsdale, S. W.; Wood, H. G.; Antholine, W. E. Evidence That an Iron-Nickel-Carbon Complex Is Formed by Reaction of CO with the CO Dehydrogenase from Clostridium Thermoaceticum. *Proc. Natl. Acad. Sci. U. S. A.* **1985**, *82* (20), 6811−6814.
(30) Ragsdale, S. W.; Ljungdahl, L. G.; DerVartanian, D. V. 13C and 61Ni Isotope Substitutions Confirm the Presence of a Nickel(III)-Carbon Species in Acetogenic CO Dehydrogenases. *Biochem. Biophys. Res. Commun.* **1983**, *115* (2), 658−665.
(31) Shanmugam, M.; Wilcoxen, J.; Habel-Rodriguez, D.; Cutsail, G. E., III; Kirk, M. L.; Hoffman, B. M.; Hille, R. 13C and 63,65Cu ENDOR Studies of CO Dehydrogenase from Oligotropha Carboxidovorans. Experimental Evidence in Support of a Copper-Carbonyl Intermediate. *J. Am. Chem. Soc.* **2013**, *135* (47), 17775−17782.
(32) Neese, F. Prediction of Molecular Properties and Molecular Spectroscopy with Density Functional Theory: From Fundamental Theory to Exchange-Coupling. *Coord. Chem. Rev.* **2009**, *253* (5−6), 526−563.
(33) Neese, F. Prediction of Electron Paramagnetic Resonance g Values Using Coupled Perturbed Hartree−Fock and Kohn−Sham Theory. *J. Chem. Phys.* **2001**, *115* (24), 11080−11096.
(34) Orio, M.; Pantazis, D. A.; Neese, F. Density Functional Theory. *Photosynth. Res.* **2009**, *102* (2−3), 443−453.
(35) Stein, M.; van Lenthe, E.; Baerends, E. J.; Lubitz, W. G- and A-Tensor Calculations in the Zero-Order Approximation for Relativistic Effects of Ni Complexes and Ni(CO)3H as Model Complexes for the Active Center of [NiFe]-Hydrogenase. *J. Phys. Chem. A* **2001**, *105* (2), 416−425.
(36) Czernuszewicz, R. S.; Fraczkiewicz, G.; Zareba, A. A. A Detailed Resonance Raman Spectrum of Nickel(II)-Substituted *Pseudomonas a Eruginosa* Azurin. *Inorg. Chem.* **2005**, *44* (16), 5745−5752.
(37) Fraczkiewicz, G.; Bonander, N.; Czernuszewicz, R. S. Metal−Ligand Interactions in Azido, Cyano and Thiocyanato Adducts of Pseudomonas Aeruginosa Met121X (X = Gly, Ala, Val or Leu) Azurins Monitored by Resonance Raman Spectroscopy. *J. Raman Spectrosc.* **1998**, *29* (10−11), 983−995.
(38) Jones, R. M.; Inscore, F. E.; Hille, R.; Kirk, M. L. Freeze−Quench Magnetic Circular Dichroism Spectroscopic Study of the "Very Rapid" Intermediate in Xanthine Oxidase. *Inorg. Chem.* **1999**, *38* (22), 4963−4970.
(39) Wongnate, T.; Sliwa, D.; Ginovska, B.; Smith, D.; Wolf, M. W.; Lehnert, N.; Raugei, S.; Ragsdale, S. W. The Radical Mechanism of Biological Methane Synthesis by Methyl-Coenzyme M Reductase. *Science* **2016**, *352* (6288), 953−958.
(40) Jiménez, H. R.; Salgado, J.; Moratal, J. M.; Morgenstern-Badarau, I. EPR and Magnetic Susceptibility Studies of Cobalt(II)- and Nickel(II)-Substituted Azurins from Pseudomonas Aeruginosa. Electronic Structure of the Active Sites. *Inorg. Chem.* **1996**, *35* (10), 2737−2741.
(41) Colpas, G. J.; Maroney, M. J.; Bagyinka, C.; Kumar, M.; Willis, W. S.; Suib, S. L.; Mascharak, P. K.; Baidya, N. X-Ray Spectroscopic Studies of Nickel Complexes, with Application to the Structure of Nickel Sites in Hydrogenases. *Inorg. Chem.* **1991**, *30* (5), 920−928.
(42) Ariyananda, P. W. G.; Kieber-Emmons, M. T.; Yap, G. P. A.; Riordan, C. G. Synthetic Analogs for Evaluating the Influence of N−H···S Hydrogen Bonds on the Formation of Thioester in Acetyl Coenzyme a Synthase. *Dalton Trans.* **2009**, *0* (22), 4359−4369.
(43) Yurkanis Bruice, P. *Organic Chemistry*, 5th ed.; Pearson Prentice Hall: Upper Saddle River, NJ, 2007.
(44) Grabarse, W.; Mahlert, F.; Duin, E. C.; Goubeaud, M.; Shima, S.; Thauer, R. K.; Lamzin, V.; Ermler, U. On the Mechanism of Biological Methane Formation: Structural Evidence for Conformational Changes in Methyl-Coenzyme M Reductase upon Substrate Binding11Edited by R. Huber. *J. Mol. Biol.* **2001**, *309* (1), 315−330.
(45) Duin, E. C.; McKee, M. L. A New Mechanism for Methane Production from Methyl-Coenzyme M Reductase As Derived from Density Functional Calculations. *J. Phys. Chem. B* **2008**, *112* (8), 2466−2482.
(46) Signor, L.; Knuppe, C.; Hug, R.; Schweizer, B.; Pfaltz, A.; Jaun, B. Methane Formation by Reaction of a Methyl Thioether with a Photo-Excited Nickel Thiolate—A Process Mimicking Methanogenesis in Archaea. *Chem. - Eur. J.* **2000**, *6* (19), 3508−3516.
(47) Han, F.-S. Transition-Metal-Catalyzed Suzuki−Miyaura Cross-Coupling Reactions: A Remarkable Advance from Palladium to Nickel Catalysts. *Chem. Soc. Rev.* **2013**, *42* (12), 5270−5298.
(48) Camasso, N. M.; Sanford, M. S. Design, Synthesis, and Carbon-Heteroatom Coupling Reactions of Organometallic Nickel(IV) Complexes. *Science* **2015**, *347* (6227), 1218−1220.
(49) Bour, J. R.; Camasso, N. M.; Meucci, E. A.; Kampf, J. W.; Canty, A. J.; Sanford, M. S. Carbon-Carbon Bond-Forming Reductive Elimination from Isolated Nickel(III) Complexes. *J. Am. Chem. Soc.* **2016**, *138*, 16105.
(50) Wilke, G. Contributions to Organo-Nickel Chemistry. *Angew. Chem., Int. Ed. Engl.* **1988**, *27* (1), 185−206.
(51) Cornella, J.; Gómez-Bengoa, E.; Martin, R. Combined Experimental and Theoretical Study on the Reductive Cleavage of Inert C−O Bonds with Silanes: Ruling out a Classical Ni(0)/Ni(II) Catalytic Couple and Evidence for Ni(I) Intermediates. *J. Am. Chem. Soc.* **2013**, *135* (5), 1997−2009.
(52) Ghosh, A.; Wondimagegn, T.; Ryeng, H. Deconstructing F430: Quantum Chemical Perspectives of Biological Methanogenesis. *Curr. Opin. Chem. Biol.* **2001**, *5* (6), 744−750.
(53) Schenker, R.; Mock, M. T.; Kieber-Emmons, M. T.; Riordan, C. G.; Brunold, T. C. Spectroscopic and Computational Studies on [Ni(Tmc)CH3]OTf: Implications for Ni−Methyl Bonding in the A Cluster of Acetyl-CoA Synthase. *Inorg. Chem.* **2005**, *44* (10), 3605−3617.
(54) Dougherty, W. G.; Rangan, K.; O'Hagan, M. J.; Yap, G. P. A.; Riordan, C. G. Binuclear Complexes Containing a Methylnickel Moiety: Relevance to Organonickel Intermediates in Acetyl Coenzyme A Synthase Catalysis. *J. Am. Chem. Soc.* **2008**, *130* (41), 13510−13511.
(55) Ito, M.; Kotera, M.; Matsumoto, T.; Tatsumi, K. Dinuclear Nickel Complexes Modeling the Structure and Function of the Acetyl CoA Synthase Active Site. *Proc. Natl. Acad. Sci. U. S. A.* **2009**, *106* (29), 11862−11866.
(56) Lipschutz, M. I.; Yang, X.; Chatterjee, R.; Tilley, T. D. A Structurally Rigid Bis(Amido) Ligand Framework in Low-Coordinate Ni(I), Ni(II), and Ni(III) Analogues Provides Access to a Ni(III) Methyl Complex via Oxidative Addition. *J. Am. Chem. Soc.* **2013**, *135* (41), 15298−15301.
(57) Ram, M. S.; Riordan, C. G.; Yap, G. P. A.; Liable-Sands, L.; Rheingold, A. L.; Marchaj, A.; Norton, J. R. Kinetics and Mechanism of Alkyl Transfer from Organocobalt(III) to Nickel(I): Implications for the Synthesis of Acetyl Coenzyme A by CO Dehydrogenase. *J. Am. Chem. Soc.* **1997**, *119* (7), 1648−1655.
(58) Smith, M. C.; Barclay, J. E.; Davies, S. C.; Hughes, D. L.; Evans, D. J. Targeting Synthetic Analogues of the Metallo-Sulfur Active Sites of Nickel Enzymes Capable of Important Catalysis. *Dalton Trans.* **2003**, *0* (21), 4147−4151.
(59) Matsumoto, T.; Ito, M.; Kotera, M.; Tatsumi, K. A Dinuclear Nickel Complex Modeling of the Nid(Ii)-Nip(i) State of the Active Site of Acetyl CoA Synthase. *Dalton Trans.* **2010**, *39* (12), 2995.
(60) McMaster, J.; Oganesyan, V. S. Magnetic Circular Dichroism Spectroscopy as a Probe of the Structures of the Metal Sites in Metalloproteins. *Curr. Opin. Struct. Biol.* **2010**, *20* (5), 615−622.
(61) Niklas, J.; Mardis, K. L.; Rakhimov, R. R.; Mulfort, K. L.; Tiede, D. M.; Poluektov, O. G. The Hydrogen Catalyst Cobaloxime: A Multifrequency EPR and DFT Study of Cobaloxime's Electronic Structure. *J. Phys. Chem. B* **2012**, *116* (9), 2943−2957.
(62) Solomon, E. I.; Pavel, E. G.; Loeb, K. E.; Campochiaro, C. Magnetic Circular Dichroism Spectroscopy as a Probe of the Geometric and Electronic Structure of Non-Heme Ferrous Enzymes. *Coord. Chem. Rev.* **1995**, *144*, 369−460.
(63) Zhang, Y.; Gebhard, M. S.; Solomon, E. I. Spectroscopic Studies of the Non-Heme Ferric Active Site in Soybean Lipoxygenase: Magnetic Circular Dichroism as a Probe of Electronic and Geometric Structure. Ligand-Field Origin of Zero-Field Splitting. *J. Am. Chem. Soc.* **1991**, *113* (14), 5162−5175.

DOI: 10.1021/acs.inorgchem.8b03546
Inorg. Chem. 2019, 58, 8969−8982

(64) Desrochers, P. J.; Telser, J.; Zvyagin, S. A.; Ozarowski, A.; Krzystek, J.; Vicic, D. A. Electronic Structure of Four-Coordinate C_{3v} Nickel(II) Scorpionate Complexes: Investigation by High-Frequency and -Field Electron Paramagnetic Resonance and Electronic Absorption Spectroscopies. *Inorg. Chem.* **2006**, *45* (22), 8930−8941.
(65) Dong, M.; Gonzalez, T. D.; Klems, M. M.; Steinberg, L. M.; Chen, W.; Papoutsakis, E. T.; Bahnson, B. J. In Vitro Methanol Production from Methyl Coenzyme M Using the Methanosarcina Barkeri MtaABC Protein Complex. *Biotechnol. Prog.* **2017**, *33* (5), 1243−1249.
(66) Bennett, R. K.; Steinberg, L. M.; Chen, W.; Papoutsakis, E. T. Engineering the Bioconversion of Methane and Methanol to Fuels and Chemicals in Native and Synthetic Methylotrophs. *Curr. Opin. Biotechnol.* **2018**, *50*, 81−93.
(67) Hagemeier, C. H.; Křer, M.; Thauer, R. K.; Warkentin, E.; Ermler, U. Insight into the Mechanism of Biological Methanol Activation Based on the Crystal Structure of the Methanol-Cobalamin Methyltransferase Complex. *Proc. Natl. Acad. Sci. U. S. A.* **2006**, *103* (50), 18917−18922.
(68) Tan, X. S.; Sewell, C.; Lindahl, P. A. Stopped-Flow Kinetics of Methyl Group Transfer between the Corrinoid-Iron-Sulfur Protein and Acetyl-Coenzyme A Synthase from Clostridium Thermoaceticum. *J. Am. Chem. Soc.* **2002**, *124* (22), 6277−6284.
(69) Tan, X.; Surovtsev, I. V.; Lindahl, P. A. Kinetics of CO Insertion and Acetyl Group Transfer Steps, and a Model of the Acetyl-CoA Synthase Catalytic Mechanism. *J. Am. Chem. Soc.* **2006**, *128* (37), 12331−12338.
(70) Barondeau, D. P.; Lindahl, P. A. Methylation of Carbon Monoxide Dehydrogenase from Clostridium Thermoaceticum and Mechanism of Acetyl Coenzyme A Synthesis. *J. Am. Chem. Soc.* **1997**, *119* (17), 3959−3970.
(71) Herbst, R. W.; Guce, A.; Bryngelson, P. A.; Higgins, K. A.; Ryan, K. C.; Cabelli, D. E.; Garman, S. C.; Maroney, M. J. Role of Conserved Tyrosine Residues in NiSOD Catalysis: A Case of Convergent Evolution. *Biochemistry* **2009**, *48* (15), 3354−3369.
(72) Davis, J. L.; Arndtsen, B. A. Sequential Insertion of Carbon Monoxide and Imines into Nickel−Methyl Bonds: A New Route to Imine Hydroacylation. *Organometallics* **2000**, *19* (23), 4657−4659.
(73) Stavropoulos, P.; Muetterties, M. C.; Carrie, M.; Holm, R. H. Structural and Reaction Chemistry of Nickel Complexes in Relation to Carbon Monoxide Dehydrogenase: A Reaction System Simulating Acetyl-Coenzyme A Synthase Activity. *J. Am. Chem. Soc.* **1991**, *113* (22), 8485−8492.
(74) Johnson, K. A.; Simpson, Z. B.; Blom, T. FitSpace Explorer: An Algorithm to Evaluate Multidimensional Parameter Space in Fitting Kinetic Data. *Anal. Biochem.* **2009**, *387* (1), 30−41.
(75) Johnson, K. A.; Simpson, Z. B.; Blom, T. Global Kinetic Explorer: A New Computer Program for Dynamic Simulation and Fitting of Kinetic Data. *Anal. Biochem.* **2009**, *387* (1), 20−29.
(76) Stoll, S.; Schweiger, A. EasySpin, a Comprehensive Software Package for Spectral Simulation and Analysis in EPR. *J. Magn. Reson.* **2006**, *178* (1), 42−55.
(77) Paulat, F.; Lehnert, N. Detailed Assignment of the Magnetic Circular Dichroism and UV−vis Spectra of Five-Coordinate High-Spin Ferric [Fe(TPP)(Cl)]. *Inorg. Chem.* **2008**, *47* (11), 4963−4976.
(78) Lehnert, N. Elucidating Second Coordination Sphere Effects in Heme Proteins Using Low-Temperature Magnetic Circular Dichroism Spectroscopy. *J. Inorg. Biochem.* **2012**, *110*, 83−93.
(79) Neese, F.; Solomon, E. I. MCD C-Term Signs, Saturation Behavior, and Determination of Band Polarizations in Randomly Oriented Systems with Spin $S \geq 1/2$. Applications to $S = 1/2$ and $S = 5/2$. *Inorg. Chem.* **1999**, *38* (8), 1847−1865.
(80) Stephens, P. J. Magnetic Circular Dichroism. *Annu. Rev. Phys. Chem.* **1974**, *25* (1), 201−232.
(81) Oganesyan, V. S.; George, S. J.; Cheesman, M. R.; Thomson, A. J. A Novel, General Method of Analyzing Magnetic Circular Dichroism Spectra and Magnetization Curves of High-Spin Metal Ions: Application to the Protein Oxidized Rubredoxin, Desulfovibrio Gigas. *J. Chem. Phys.* **1999**, *110* (2), 762−777.
(82) Lehnert, N.; George, S. D.; Solomon, E. I. Recent Advances in Bioinorganic Spectroscopy. *Curr. Opin. Chem. Biol.* **2001**, *5* (2), 176−187.
(83) Schneider, S. S. B. Piepho and P. Schatz: Group Theory in Spectroscopy With Applications to Magnetic Circular Dichroism, Aus Der Reihe: Wiley Interscience Monographs in Chemical Physics, John Wiley + Sons, New York, Chichester, Brisbane, Toronto, Singapore 1983. 634 Seiten, Preis: £ 65.75. *Berichte Bunsenges. Für Phys. Chem.* **1984**, *88* (10), 1023−1023.
(84) Shearer, J.; Peck, K. L.; Schmitt, J. C.; Neupane, K. P. Cysteinate Protonation and Water Hydrogen Bonding at the Active-Site of a Nickel Superoxide Dismutase Metallopeptide-Based Mimic: Implications for the Mechanism of Superoxide Reduction. *J. Am. Chem. Soc.* **2014**, *136* (45), 16009−16022.

DOI: 10.1021/acs.inorgchem.8b03546
Inorg. Chem. 2019, 58, 8969−8982